Advanced Modeling of Shrinkage Porosity and Application to Mn-Steel Castings

Vahid Khalajzadeh and Christoph Beckermann

Department of Mechanical Engineering, University of Iowa
Iowa City, IA 52242, USA

ABSTRACT

Porosity due to solidification shrinkage is a troublesome defect in steel casting. It limits the performance of cast components by adversely affecting the steel's mechanical, fatigue, and creep properties. By reliably predicting porosity in casting process simulation, it can be minimized or eliminated. Here recent advancements for predicting porosity are summarized. The development, validation and application of a modeling approach to predict macro-shrinkage porosity, surface sink and micro-shrinkage porosity is presented. The model was developed to more accurately predict the location, amount and appearance of porosity. Porosity predictions are demonstrated for simple casting geometries, and for more complex experimental castings. The comparisons to Mn-steel experiments demonstrate the promise and capabilities of the model to predict surface sink, internal shrinkage porosity and centerline shrinkage porosity. The predicted porosity location and appearance more closely mirrors observed porosity than current simulation models.

Keywords: Computational model, surface sink, shrinkage porosity, feeding flow, liquid pressure, pore nucleation, metal casting

1. INTRODUCTION

Shrinkage porosity defects significantly reduce the strength, fatigue life, and creep capability of cast components [1, 2, 3]. As numerous critical parts in aerospace and automotive industries are manufactured through the casting processes, it is important to ensure these parts are free of defects and are structurally sound. Shrinkage porosity defects form when there is insufficient liquid metal available to compensate for the volume contraction in a solidifying region. If the liquid feed-path is cut off, shrinkage defects in the form of surface sinks and internal porosities will occur as shown in Figure 1. Researchers have investigated mathematical models described by the fundamental physics of porosity formation. By implementing these models in standard casting simulation software, engineers can design optimal casting rigging systems.

Most models for predicting porosity formation originate from the one-dimensional (1D) model of Piwonka and Flemings [4] and the two-dimensional (2D) model of Kubo and Pehlke [5]. Over the past two decades, several advances in the development of porosity models for castings have been made. Pequet et al. [6] developed a three-dimensional (3D) model that applies a dynamic mesh refinement algorithm for the semi-solid mushy zone. The 3D multi-phase model developed by Carlson et al. [7-9] predicts the feeding velocity, liquid pressure, and porosity distributions during alloy solidification. However, it does not consider the formation of surface sinks. The model by Reis et al. [10,11] predicts the formation of surface sinks and internal porosity. In this model, a

volume-of-fluid (VOF) approach is used to track the liquid surface movement during solidification. Their results showed that in alloys with a long freezing range, shrinkage defects tend to form on the exterior surface of a casting, while in the short freezing range alloys, such defects tend to appear in the form of internal porosities [10].

Despite some success of modeling to predict shrinkage porosity in castings, a comprehensive model that predicts surface sinks, internal porosity, mass feeding and centerline shrinkage porosity in castings is lacking.
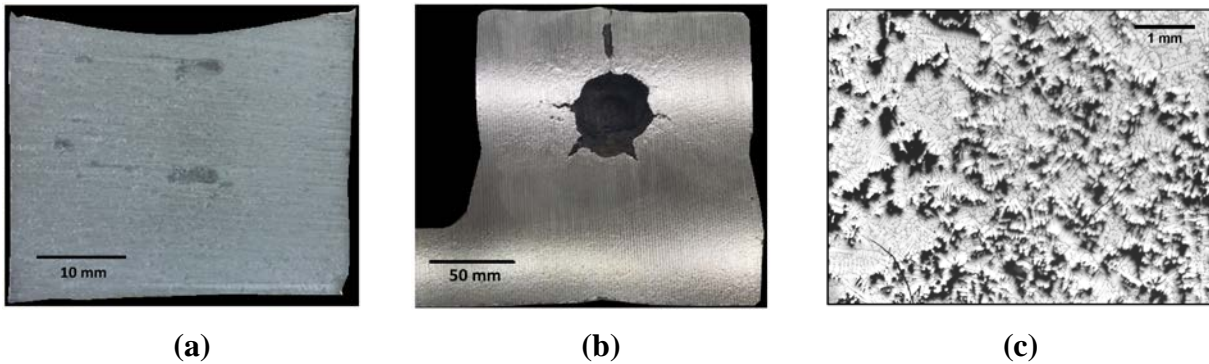

| (a) | (b) | (c) |

Figure 1. Surface sink and porosity defects caused by shrinkage: (a) surface depression or surface sink, (b) internal macro-shrinkage porosity, (c) internal micro-shrinkage porosity

Here a computational model for the prediction of surface sinks and internal shrinkage defects in castings is presented. Transient temperature and solid fraction fields are obtained from casting simulation software. A computational model is developed to predict the nucleation and growth of the shrinkage porosity using the casting simulation results as its input. The model solves the equations describing the shrinkage driven feeding flow to obtain the liquid pressure and velocity, and the pore-fraction distribution in the casting. The model capabilities are demonstrated by applying it to several examples and experimental cases.

2. COMPUTATIONAL MODEL

A schematic diagram of a solidifying casting volume described by the porosity model is shown in Figure 2. Multiple porosity regions of porosity can form simultaneously with boundary conditions at the casting surface and on volumes of porosity indicated in Figure 2(a). The model allows for a control volume in the casting to be composed of three phases: solid (s), liquid (ℓ) and porosity (p). Using g to denote the volume fraction of a given phase, and the phases indicated by subscripts, the volume fractions must satisfy $g_\ell + g_s + g_p = 1$ as shown schematically in Figure 2(b). Key assumptions in the model are:

- Solid and porosity phases are stationary; they cannot move during solidification.
- Flow movement only occurs by shrinkage in the system so buoyancy-driven flow during solidification is neglected.
- Density is temperature-dependent above the solidus temperature and is assumed constant when the metal is solid; the density the matter inside of shrinkage pores is neglected.

Additional details of model development with describing equations and procedures for porosity prediction are given in the following sections.
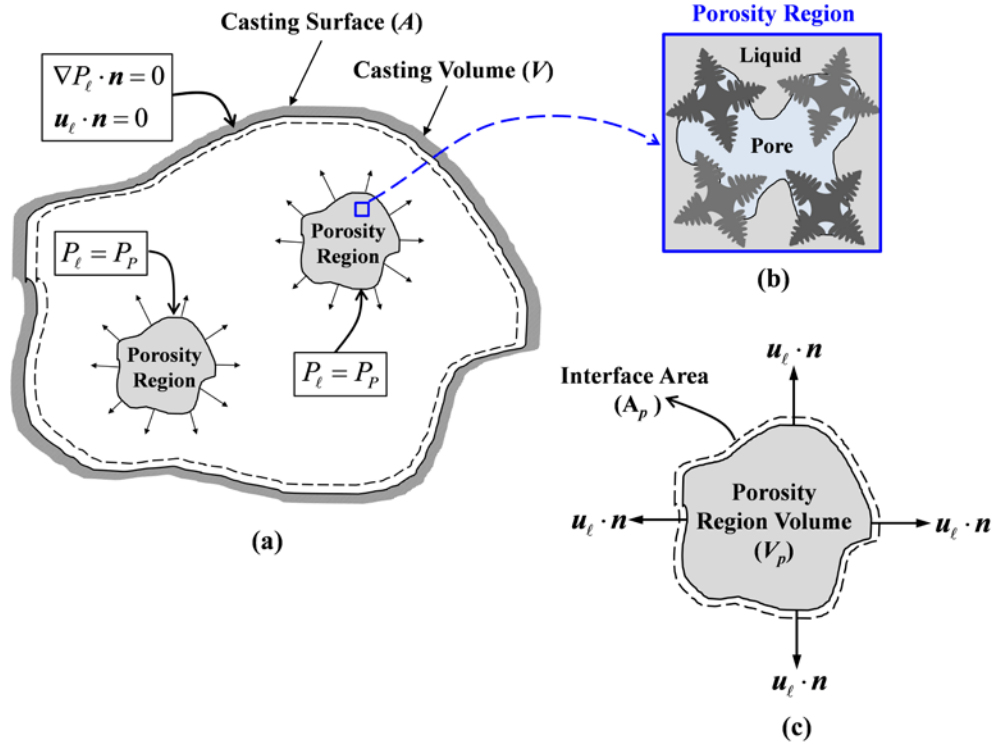

Figure 2. (a) Schematic diagram of solidifying casting volume with regions of porosity, (b) a representative volume from a region where porosity is forming, and (c) diagram of a region where porosity is forming.

2.1. Continuity and Momentum Equations

Since the solidifying mushy zone is composed of solid, liquid and porosity phases, mass is conserved according to a mixture continuity equation given by

$$\frac{\partial \overline{\rho}}{\partial t} + \nabla \cdot \left(\rho_\ell \boldsymbol{u}_\ell \right) = 0 \tag{1}$$

where $\overline{\rho}$ is the metal mixture density which is defined from density vs. temperature curve and $\boldsymbol{u}_\ell$ is the superficial velocity vector, which is defined as $\boldsymbol{u}_\ell = g_\ell \boldsymbol{v}_\ell$ where $\boldsymbol{v}_\ell$ is the liquid velocity vector. Additionally, the model assumes that the feeding flow in the mushy zone is a creeping flow and follows the assumptions for flows in porous media. For such flows the momentum equation is given by Darcy's law,

$$\nabla P_{\ell,T} = -\frac{\mu_\ell \boldsymbol{u}_\ell}{K} + \rho_\ell \boldsymbol{g} \tag{2}$$

where $P_{\ell,T}$ is the total liquid pressure, μ_ℓ is the melt dynamic viscosity, K is the permeability of the solidifying metal and $\boldsymbol{g}$ is the gravity vector. Equation (2) is also used as the momentum equation for the flow in pure liquid regions of the casting, where the solid fraction is zero, by

3

setting the permeability to a large value, K_{max}. The total liquid pressure ($P_{\ell,T}$) is defined as the sum of dynamic liquid pressure (P_ℓ) and the hydrostatic pressure (P_h) so that $P_{\ell,T} = P_\ell + P_h$. Applying the gradient operator to this equation

$$\nabla P_{\ell,T} = \nabla P_\ell + \nabla P_h \tag{3}$$

where the hydrostatic pressure gradient (∇P_h) is given by $\nabla P_h = \rho_\ell \boldsymbol{g}$. Combining Eq. (2) and (3) the gravity terms cancel and Eq. (2) is simplified to

$$\nabla P_\ell = -\frac{\mu_\ell \boldsymbol{u}_\ell}{K} \tag{4}$$

It is assumed that the permeability of the solidifying metal K is a function of solid fraction (g_s) and described by the Kozeny–Carman equation

$$K = K_0 \frac{(1-g_s)^3}{g_s^2} \tag{5}$$

where K_0 is a constant permeability coefficient in the current study. To avoid numerical problems, such as dividing by zero in Eq. (4), minimum and maximum allowable values for K are defined as K_{min} and K_{max}, respectively. These two parameters are alloy dependent and are determined here in a parametric study described below.

A constant reference liquid pressure is needed to determine a solution for Eq. (4). Here it is assumed that P_ℓ within regions having porosity is equal to the pore pressure, i.e. $P_\ell\big|_{Porosity} = P_p$. The value of the pore pressure P_p depends here on location; at the atmosphere-metal interface it is assumed to be $P_p = P_{atm}$, while at the mold-metal interface $P_p = P_{mold}$ and for internal porosity $P_p = 0$.

Since it is assumed that ρ_ℓ is constant during solidification, Eqs. (1) and (4) can be combined to form an equation for determining the pressure P_l throughout the casting during solidification

$$\nabla \cdot \left(-\frac{K}{\mu_\ell} \nabla P_\ell \right) = -\frac{1}{\rho_\ell} \frac{\partial \overline{\rho}}{\partial t} \tag{6}$$

Eq. (6) has a form known as a Poisson Equation. It is an elliptical partial differential equation requiring two boundary conditions to have a valid solution. Here one boundary condition is determined by the condition to solve Eq. (4) such that $P_\ell\big|_{Porosity} = P_p$, and the second is provided by the zero-mass flux condition at the casting walls, which is $(\boldsymbol{u}_\ell \cdot \boldsymbol{n})_{Surface} = (\nabla P_\ell \cdot \boldsymbol{n})_{Surface} = 0$. These boundary conditions are shown schematically in Figure 2. Using these boundary conditions, the pressure distribution P_ℓ in the casting can be determined by solution of Eq. (6). The expanded form of Eq. (6) in 3D Cartesian coordinates is

$$\frac{\partial}{\partial x}\left(\frac{K}{\mu_\ell} \frac{\partial P_\ell}{\partial x} \right) + \frac{\partial}{\partial y}\left(\frac{K}{\mu_\ell} \frac{\partial P_\ell}{\partial y} \right) + \frac{\partial}{\partial z}\left(\frac{K}{\mu_\ell} \frac{\partial P_\ell}{\partial z} \right) = \frac{1}{\rho_\ell} \frac{\partial \overline{\rho}}{\partial t} \tag{7}$$

which is discretized and solved using a finite volume approach. After P_ℓ is calculated, the total pressure ($P_{\ell,T}$) is calculated using

$$P_{\ell,T} = P_\ell + P_h \tag{8}$$

where P_h is the hydrostatic pressure given by $P_h = \rho_\ell g(z_{max} - z)$ and $(z_{max} - z)$ is the hydrostatic head from a reference height of z_{max}. The velocity distribution in the casting due to the shrinkage driven flow is determined by solving Eq. (4) for u_l as given below

$$\boldsymbol{u}_\ell = -\frac{K}{\mu_\ell} \nabla P_\ell \tag{9}$$

The velocity components are given from Eq. (9) by:

$$u_\ell = -\frac{K}{\mu_\ell}\left(\frac{\partial P_\ell}{\partial x}\right) \quad ; \quad v_\ell = -\frac{K}{\mu_\ell}\left(\frac{\partial P_\ell}{\partial y}\right) \quad ; \quad w_\ell = -\frac{K}{\mu_\ell}\left(\frac{\partial P_\ell}{\partial z}\right) \tag{10}$$

where u_ℓ, v_ℓ, w_ℓ are the superficial liquid velocity components in x, y, z directions. Details on pore nucleation and growth are described next.

2.2. Pore Nucleation

The calculated pressure field is used to predict the nucleation of a pore in the liquid metal. Pore nucleation is assumed to occur heterogeneously at pre-existing nucleation sites in the mushy zone. Pores can only grow if the energy needed to overcome the capillary pressure is provided. Since gas porosity is not considered in this work, this nucleation energy is provided by large pressure drops due to flow resistance in the solidifying mush in the absence of any dissolved gas in the casting. Considering this nucleation mechanism, the pore nucleation criterion is given by the inequality form of the Young-Laplace equation

$$P_p - P_{\ell,T} \geq P_\sigma \tag{11}$$

where, $P_{\ell,T}$ is the total liquid pressure which is defined as $P_{\ell,T} = P_\ell + \rho_\ell g(z_{max} - z)$; P_P is the pore pressure, and P_σ is the capillary pressure due to surface tension. According to experimental observations [12], surface sinks and shrinkage porosity tend to nucleate first in areas with low solid fractions, as in the case of the hot spot in Figure 1(b). In other words, during solidification pores nucleate preferentially in regions with more liquid. As a result, the model presented here assumes that the capillary pressure in the solidifying metal P_σ is a linear function of the solid-fraction g_s

$$P_\sigma = P_{\sigma,0} \times g_s \tag{12}$$

where $P_{\sigma,0}$ is a constant coefficient which is an alloy dependent parameter. Using Eq. (12) in Eq. (11) the nucleation criterion is more easily met if the solid fraction is low. Furthermore, it is also assumed that after nucleation, due to the small surface curvature at the pore-liquid interfaces, P_σ in the porosity region becomes negligibly small. Therefore, it is assumed that $P_\sigma = 0$ in regions

with porosity.

As mentioned above, surface sinks and internal porosity start forming or nucleate in locations where the solid fraction is the lowest. On the surface of a casting, it is possible that this lowest solid fraction occurs simultaneously at multiple locations. Among those locations, surface sinks form only where the metallostatic head pressure is relatively low. For internal porosity, there can also be multiple locations or computational cells where the solid fraction is uniformly low. An example would be a large internal region at the center of a casting section that is still fully liquid. Again, within such a region of uniform low solid fraction, porosity is found to nucleate only at the location where the metallostatic head pressure is the lowest. Based on these observations, the nucleation criterion (Eq. 11) is applied using a parameter Π that incorporates the effects of both solid fraction and metallostatic head pressure to determine which cells will form porosity. The parameter Π is

$$\Pi = P_{\ell,T} - \left(P_p - P_\sigma \right) \tag{13}$$

with nucleation taking place at those locations in the casting where the Π parameter is lowest. To make the porosity calculations independent of rounding errors and the time-step used in the numerical simulations, porosity is nucleated in all computational cells where the Π value falls within a small dimensionless interval ε_{nuc} according to

$$\left| \frac{\Pi - \Pi_{min}}{\Pi_{max} - \Pi_{min}} \right| < \varepsilon_{nuc} \tag{13}$$

where Π_{min} is the minimum and Π_{max} is the maximum Π value in the casting. A suitable value for ε_{nuc} that gives good agreement between observed and calculated porosity nucleation patterns is determined below in a parametric study. Physically, ε_{nuc} controls the size of a region where porosity nucleates. Once porosity nucleates in a computational cell, it becomes an "active" cell.

2.3. Surface Coherency and Porosity Location

The model does not distinguish between surface sinks and internal porosity. Both are treated as shrinkage porosity. Observations [12] indicate that the two types of porosity do not evolve simultaneously, but in a two-stage process: first surface sinks develop and, then, internal porosity forms. The transition between the two stages is assumed to occur when the solid fraction everywhere on the casting surface exceeds a certain critical value, $g_{s,sur}$. Shown in Figure 3, when the solid fraction at the surface is below this critical value, the equiaxed solid dendrites and the melt can both move to accommodate the volume deficit due to solidification shrinkage and a surface sink forms. Once the solid fraction everywhere on the surface is above $g_{s,sur}$, the dendrites form a coherent and rigid solid network that prevents any further displacement of the surface. Then, the solidification shrinkage must be accommodated by internal porosity. Theoretically, the melt between the rigid dendrites at the casting surface could still move, but such movement would be resisted by relatively high capillary forces.

Porosity is nucleated only if there are no active computational cells already present in the computational domain. An active cell is defined as a cell where porosity is currently growing (see also below). As long as there is a possibility of surface sinks forming, i.e., if there are surface cells where $g_s < g_{s,sur}$, the nucleation calculations are performed only for surface cells and internal cells are ignored. As soon as $g_s > g_{s,sur}$ everywhere on the surface of the casting, internal computational cells where the Π parameter satisfies Eq. (13) are activated.

(a)   **(b)**
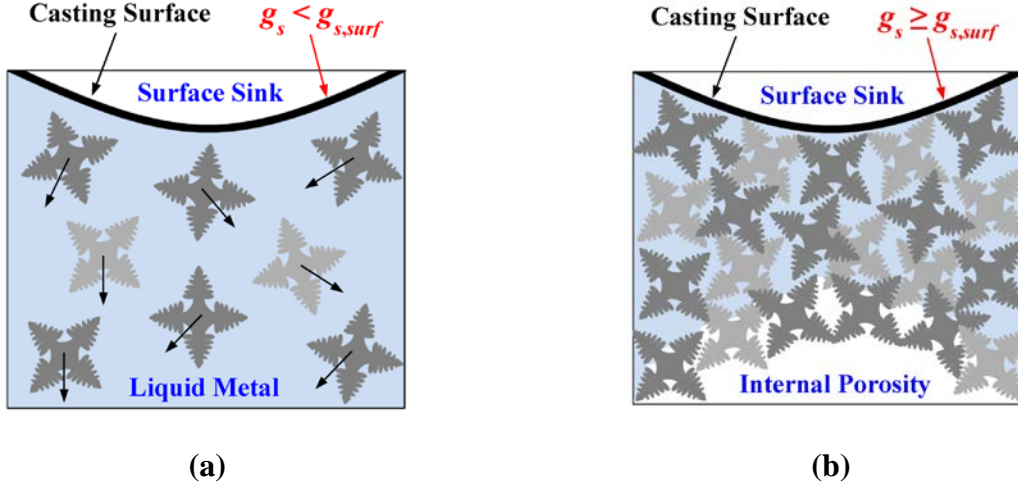
Figure 3. Schematic diagram of surface sink and internal porosity formation: (a) for $g_s < g_{s,sur}$ the dendrites and the melt can move and a surface sink forms; (b) once $g_s \geq g_{s,sur}$ dendrites form a coherent and rigid network; the surface stops moving and internal porosity forms inside of the casting.

2.4. Pore Growth

As shown in Figure 2(a), multiple regions of porosity can nucleate and grow in a casting. Each region is a grouping of connected computational cells having $g_p > 0$ in the model (as discussed below). The volume of a given region of the casting with porosity forming is V_p. Once nucleated, the growth of porosity within a region of the casting is calculated from the pore growth rate ($d\overline{g}_p/dt$), which is determined applying the mass conservation law at the interface of the pore-liquid interface. In Figure 2(c) a region with porosity having volume of V_p and the interface area of A_p is shown. The mass conservation law for the region with porosity is given by

$$\int_{V_P} \left(\frac{\partial \overline{\rho}}{\partial t} \right) dV + \int_{A_P} (\rho_\ell \boldsymbol{u}_\ell) \cdot \boldsymbol{n} \, dA = 0 \tag{14}$$

where $\overline{\rho}$ is the alloy mixture density, $\boldsymbol{u}_\ell$ is the superficial velocity vector and $\boldsymbol{n}$ is the normal vector to the interface. Two approaches are commonly used to define $\overline{\rho}$ during solidification. In one approach, a two-phase mixture of solid and liquid ($\overline{\rho}^{SL}$) is used. In the other a three-phase

mixture of solid, liquid, and porosity ($\bar{\rho}$) is used. The two-phase mixture density, $\bar{\rho}^{SL}$, is defined as $\bar{\rho}^{SL} = \rho_s g_s^{SL} + \rho_\ell g_\ell^{SL}$ where $g_s^{SL} + g_\ell^{SL} = 1$. The three-phase mixture density, $\bar{\rho}$, is defined by $\bar{\rho} = \rho_s g_s + \rho_\ell g_\ell + \rho_p g_p$ where $g_\ell + g_s + g_p = 1$. Combining these two approaches, and assuming $g_s^{SL} = g_s$ and $\rho_p \ll \rho_s, \rho_\ell$, the following equation is derived for $\bar{\rho}$ as a function of $\bar{\rho}^{SL}$, ρ_ℓ, and g_p

$$\bar{\rho} = \bar{\rho}^{SL} - \rho_\ell g_p \tag{15}$$

By replacing $\bar{\rho}$ in Eq. (14) with Eq. (15), the change of the average pore volume fraction ($\bar{g}_p$) in a porosity region can be calculated from the knowledge of the temperature and feeding flow distributions from the simulation and the solid-liquid mixture density ($\bar{\rho}^{SL}$) vs. temperature curve according to:

$$\frac{d\bar{g}_p}{dt} = \frac{1}{\rho_\ell V_p} \int_{V_P} \left(\frac{\partial \bar{\rho}^{SL}}{\partial t} \right) dV + \frac{1}{V_p} \int_{A_P} \boldsymbol{u}_\ell \cdot \boldsymbol{n} \, dA \tag{16}$$

where, V_p is the total volume of the pore forming region. In order to predict the local porosity distribution in the casting additional assumptions must be made, because the present model is intended to be simple. The main assumption that is made in the present porosity growth model is that the solidification shrinkage volume of a porosity region for each numerical time interval is distributed evenly over all active computational cells where porosity is currently growing. With this assumption, the time rate of change in the local pore volume fraction (g_p) is the same for each active cell and can be calculated from

$$\frac{dg_p}{dt} = \left(d\bar{g}_p / dt \right) \big/ g_{active} \tag{17}$$

where $g_{active} = V_{active} / V_P$ is the volume fraction of active cells in the porosity region, in which V_{active} is the total volume of all active cells in the porosity region.

The pore volume fraction in each active computational cell is initiated as zero and is typically allowed to increase until the cell becomes empty of liquid, i.e., when $g_s + g_p = 1$. The latter condition would, however, result in the local pore fraction never being able to approach unity ($g_p = 1$). A pore fraction of unity corresponds to a surface sink or large internal hole that is free of solid, both of which are readily possible. For the pore volume fraction to reach unity, the previously grown solid at that location must have been moved or pushed away by the growing porosity, which is frequently referred to as mass feeding. Mass feeding can only occur if the solid fraction is below a so-called coherency solid fraction $g_{s,coh}$, i.e., when $g_s < g_{s,coh}$. Above the coherency solid fraction, the dendrites form a rigid solid network that cannot move. The coherency solid fraction can be expected to take the same value as the previously introduced critical value $g_{s,sur}$ at which surface sinks stop forming. With these considerations, the maximum pore volume fraction, $g_{p,max}$, is given by

$$g_{p,\max} = \begin{cases} 1 & \text{for} \quad g_s < g_{s,coh} \\ 1 - g_s & \text{for} \quad g_s \geq g_{s,coh} \end{cases} \tag{18}$$

The two critical solid fractions $g_{s,sur}$ and $g_{s,coh}$ are retained as separate parameters to allow for additional flexibility in tuning the model.

A computational cell that reaches the maximum pore fraction becomes inactive. Once there are no more active cells present in the computational domain, but solidification is not yet complete, new cells must be activated to accommodate the shrinkage. Such activation is accomplished using the same Π parameter introduced in the previous subsection, but only for those computational cells that neighbor a cell with porosity already present. The latter condition ensures that porosity grows by spreading in layers around regions with preexisting porosity, rather than by nucleating in other regions of the wedge where no porosity is present. In other words, spreading of existing porosity is assumed to be easier than nucleating new porosity. Hence, cells that neighbor a cell where $g_p \neq 0$ are activated when their Π parameter falls within the interval

$$\left| \frac{\Pi - \Pi_{\min}}{\Pi_{\max} - \Pi_{\min}} \right| < \varepsilon_{layer} \tag{19}$$

The small dimensionless number ε_{layer} is a model parameter that controls the rate of spreading of porosity regions. For model tuning flexibility, it is allowed to take a different value than ε_{nuc}.

The porosity algorithm described above is applied to regions of porosity throughout the casting. These regions must be identified and tracked throughout the solidification process. A search algorithm is used to identify all porosity regions in the casting. In the image processing literature, the algorithm used is termed the "connected-component labeling" algorithm. This approach also finds applications in other technologies such as computer graphics, CAD modeling software and mapmaking [16], and it is used to identify subsets of connected regions in an image having any dimension [16]. For example, a 2D image might be an x-ray, and a 3D image might be a computed tomography scan of a volume. In applying this method to porosity modeling, the porosity field is converted to a binary field first using a thresholding function

$$\textit{Binary Value} = \begin{cases} 0 & g_p = 0 \\ 1 & g_p > 0 \end{cases} \tag{23}$$

If a cell has no porosity ($\textit{Binary Value} = 0$) the cell is termed a background cell. While cells with porosity ($\textit{Binary Value} = 1$) are foreground cells and the connected regions in the foreground are determined and grouped. By the search algorithm as applied from reference [16], the porosity regions are identified throughout the entire casting. Then the liquid pressure in the porosity regions are forced to the values of pore pressure P_p discussed earlier ($P_p = P_{atm}$ at the atmosphere-metal interface, $P_p = P_{mold}$ at the mold-metal interface and $P_p = 0$ for internal porosity). Then feeding flow equations (7) and (9) are solved to obtain the pressure and velocity distributions in the casting,
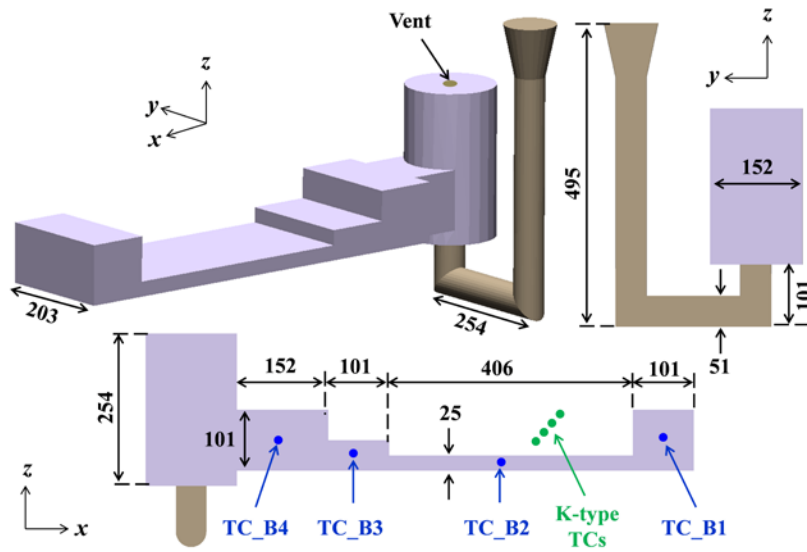
respectively. Finally, for each region of porosity, Eq. (17) is calculated to determine the pore growth (dg_p/dt) and the porosity formed.

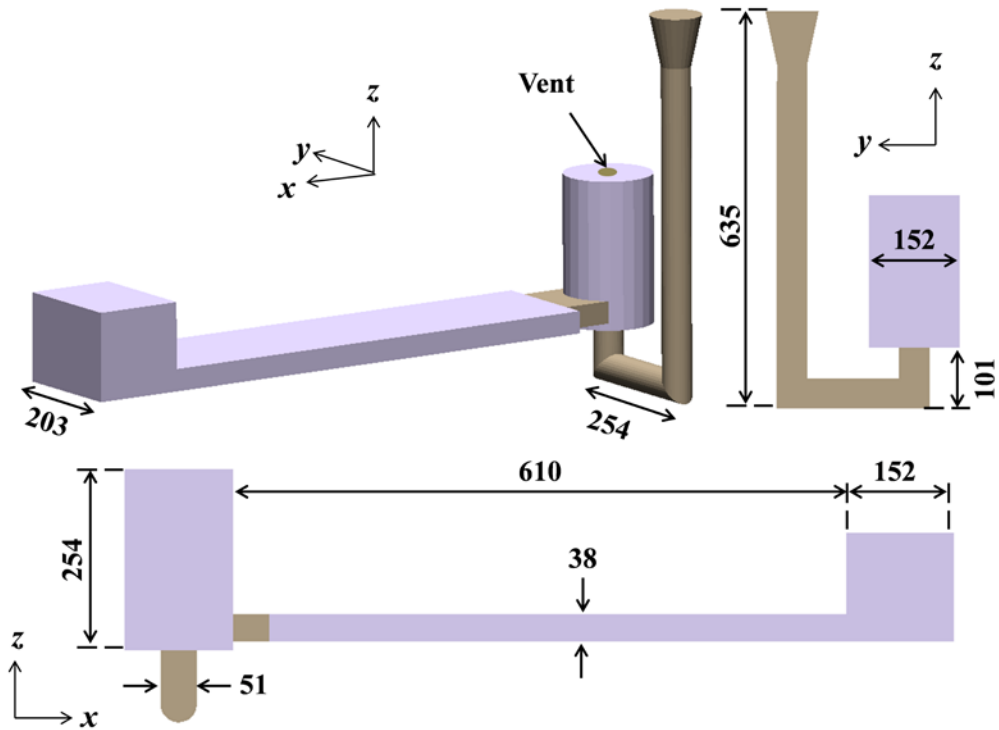## 3. EXPERIMENTAL STUDY FOR MODEL DEMONSTRATION

Two experiments were designed using casting simulation to better understand porosity formation in steel castings. A Manganese-steel (Mn-steel) having approximately 13 wt% Mn was used in the experiments. The compositions for the steel used in the experiments are given in Table 1. Solidification shrinkage for this Mn-steel is somewhat large, and porosity is more problematic for this alloy. The experimental casting geometries are presented in Figure 4, where both are plate-like shapes with block sections at the end of the plates to generate hot spots. Molds used in the experiments are made of Olivine sand. Use of this sand prevents defects that might occur using silica sand, where SiO_2 reacts with MnO in the steel to form a $MnSiO_3$ slag and burn on defects. Several thermocouples (TCs) are placed at several locations in the castings and sand molds. These provide measurements of the cooling of the castings during solidification and are used to calibrate the accuracy of the simulations. Thermocouples in the mold are inserted through the top of the cope section at 6, 12, 18 and 24 mm distances from the mold-metal interface. Type-B thermocouples are used to measure the cooling of the steel. These are inserted through the cope into the mold cavity, and their data is recorded throughout filling and during solidification.

Table 1- Mn-Steel composition given in weight percent (Wt Pct)

Element	Experiment 1 Amount (Wt Pct)	Experiment 2 Amount (Wt Pct)
C	1.1	1.13
Mn	13.2	12.99
Si	0.65	0.68
P	0.042	0.050
S	0.005	0.004
Cr	0.33	0.46
Ni	0.11	0.10
Mo	0.84	0.36
Al	0.030	0.052
Cu	0.11	0.10
Ti	0.00	0.20
Fe	balance	balance

Figure 4. Mn-Steel casting geometries: (a) Experiment 1 with TC locations in blue and green, and (b) Experiment 2; all dimensional units in the diagrams are millimeter (mm).

Analyzing the thermocouple measurements for Experiment 1 using the procedures described in [13], the measured solidus and liquidus temperatures of Mn-Steel alloy were determined to be $T_{sol} = 1250\,°C\,(2300\,°F)$ and $T_{liq} = 1396\,°C\,(2545\,°F)$, respectively. The temperature data from Experiment 1 were also used to perform inverse modeling to determine temperature dependent thermo-physical properties for use in casting simulations. In this process, the softwares IDS [14] and JMatPro™ [15] are used to generate an initial dataset for temperature-dependent properties. Then these properties are adjusted while comparing measured and simulated temperature data until simulation TC results agree best with the measurements. Similarly the interfacial heat transfer coefficient (IHTC) curve is determined using an iterative trial-and-error procedure comparing measurements and simulations. The final IHTC as a function of temperature is a constant $1100\ \mathrm{W/m^2K}$ for temperatures above $1350\,°C\,(2462\,°F)$, then below $1350\,°C$ the IHTC decreases to $200\ \mathrm{W/m^2K}$ at liquidus temperature, and then it drops to $150\ \mathrm{W/m^2K}$ at around $800\,°C\,(1472\,°F)$ and remains constant at lower temperatures.
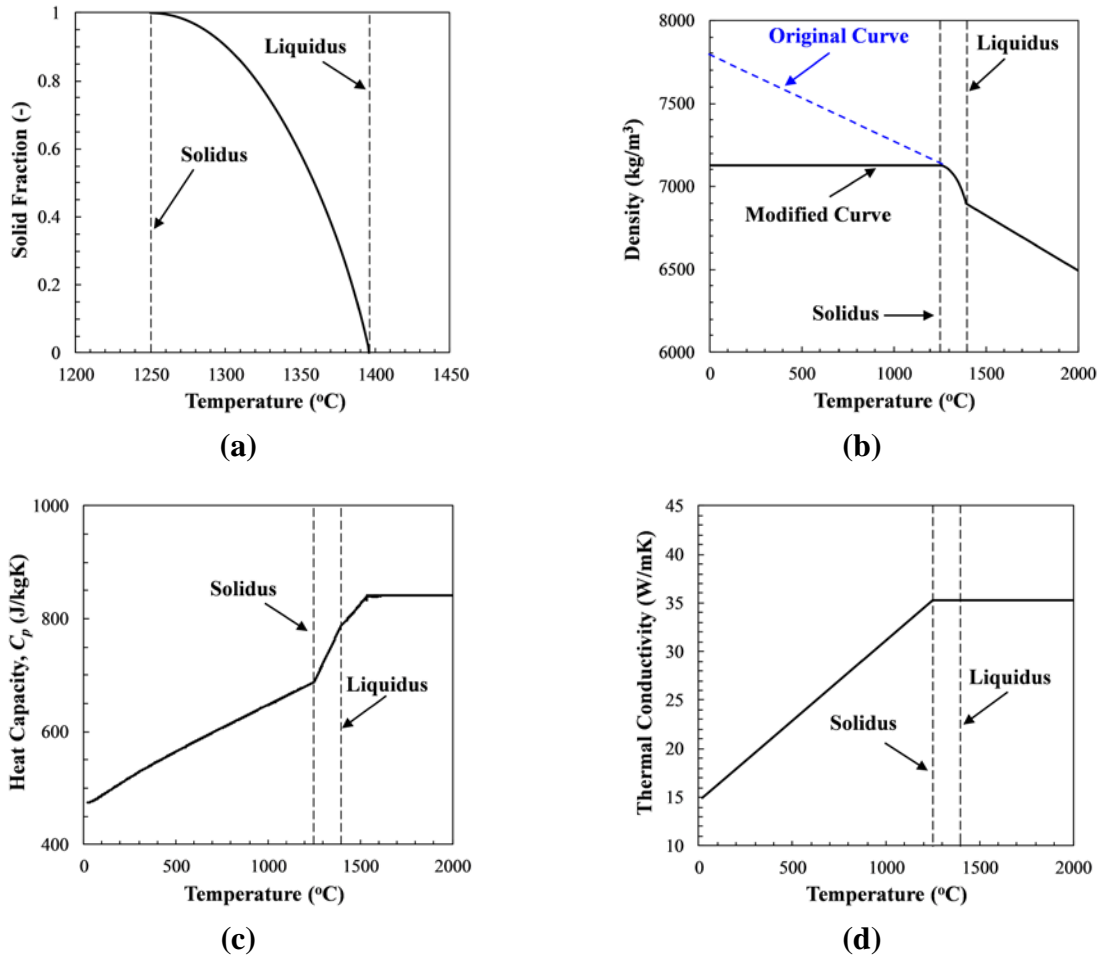
Figure 5. Manganese-steel (Mn-steel) alloy temperature-dependent properties (a) solid-fraction, (b) density, (c) heat capacity, and (d) thermal conductivity.

The properties determined by this procedure for the Mn-Steel used in the experiments are shown in Figure 5. Note in Figure 5(a) and (b) that as the temperature decreases, the solid-fraction and density increases; while for example, the thermal conductivity (Figure 5(d)) is at first constant above the liquidus temperature and decreases below solidus as the temperature decreases. For the density curve, it is assumed that the alloy does not contract below solidus.

Figure 6 provides the temperature dependent Olivine sand thermal conductivity and heat capacity. The density of Olivine sand is 1830 kg/m^3. The Mn-Steel latent heat of fusion used here is 203 kJ/kg , which produced the best agreement between simulations and measured TCs. Using the properties developed for the Mn-Steel alloy, the temperature data from the experiments were accurately simulated. In Figures 7 and 8, temperature and cooling rate data are compared for the measurements and simulations in the mold and the steel, respectively. The thermocouple results confirm the validity of the thermal simulations. This is an important first step to accurately predict the porosity.

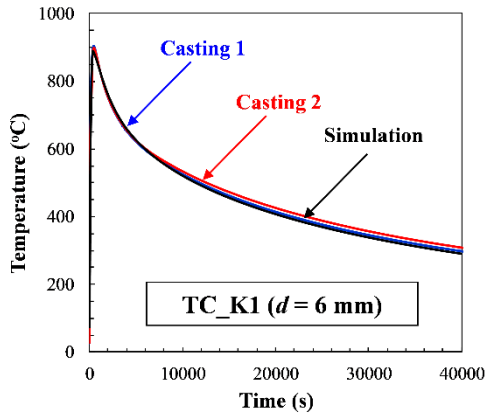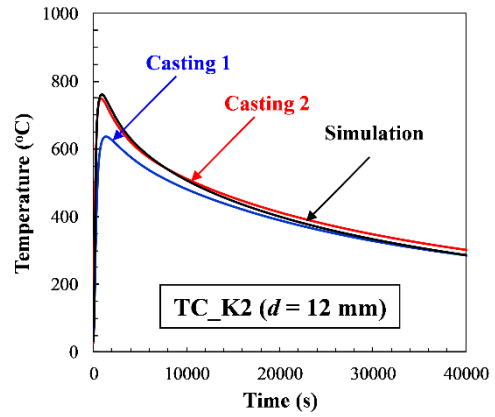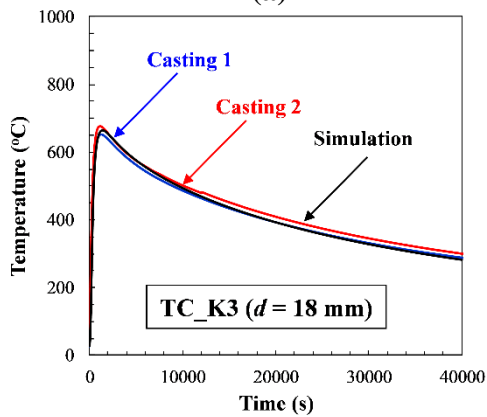(a)   (b)
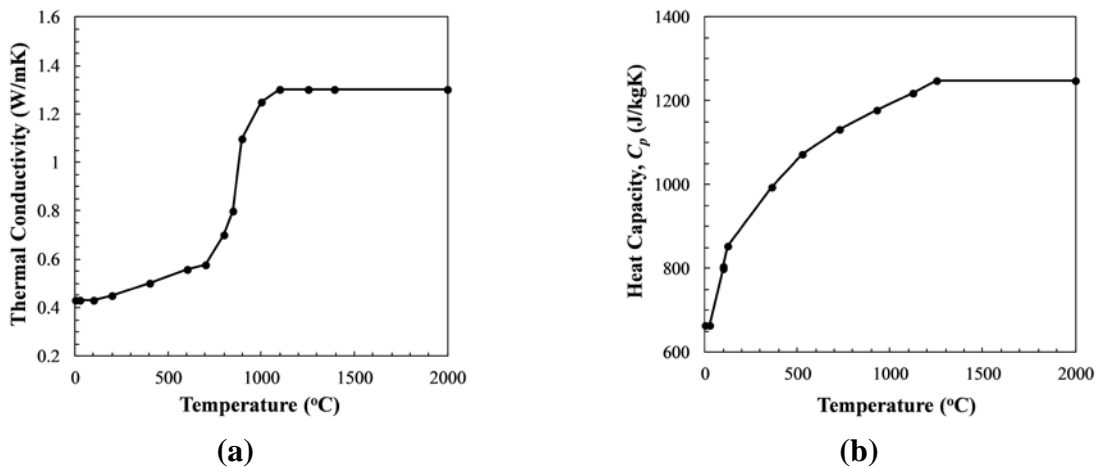
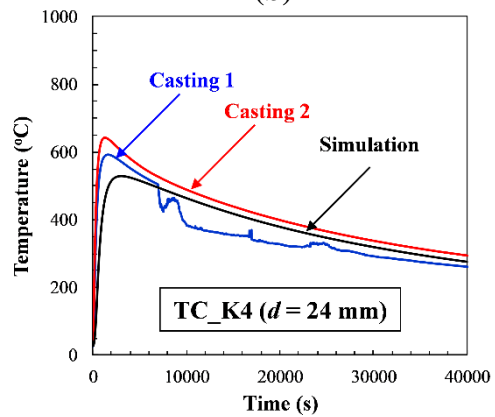Figure 6. Olivine sand temperature dependent properties (a) thermal conductivity and (b) heat capacity.

Figure 7. Comparison of thermocouple measurements and simulation results in the olivine sand mold (a) temperature vs. time at the TC_K1 location, (b) at the TC_K2 location, (c) at the TC_K3 location, and (d) at the TC_K4 location.
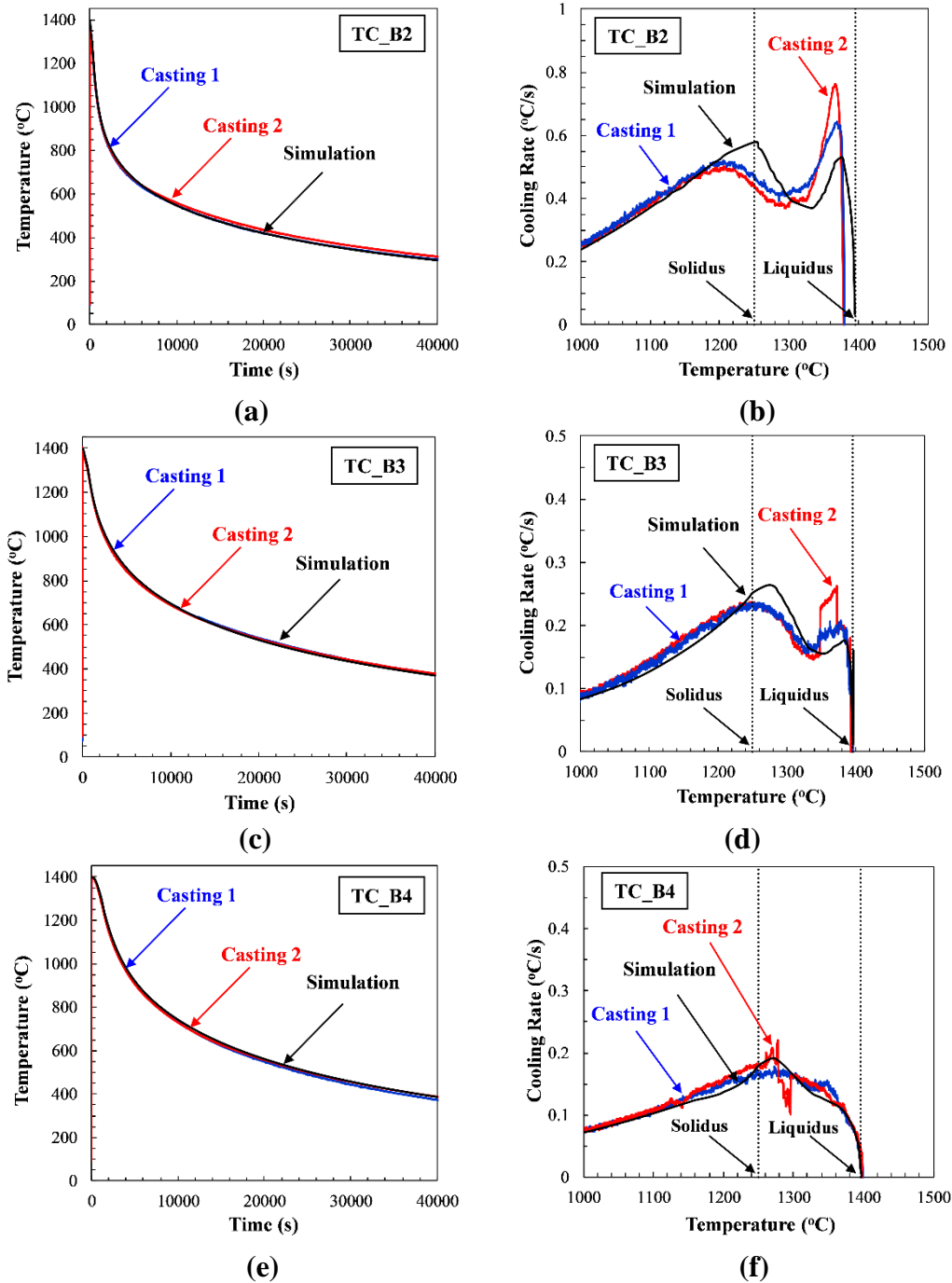
Figure 8. Comparison of Mn-steel thermocouple measurements and simulation results (a) temperature vs. time at the TC_B2 location, (b) cooling rate vs. temperature at the TC_B2 location, (c) temperature vs. time at the TC_B3 location, (d) cooling rate vs. temperature at the TC_B3 location, (d) temperature vs. time at the TC_B4 location, (e) cooling rate vs. temperature at the TC_B4.

15

4. MODEL RESULTS AND DISCUSSION

The model is applied first to three simple test castings to illustrate its capabilities. These test cases are: a block with a single feeding zone, a riser with surface sink followed by internal porosity, and a block with two feeding zones. Following the presentation of these test cases, the model is applied to the two experimental Manganese Steel (Mn-Steel) castings presented in the previous section, and the predicted porosity results are compared with observations of the porosity in the experimental castings.

4.1 Model Testing and Examples

Before applying the model to real castings, it is important to verify that the porosity model performs as expected for simple cases. Thus, three cases with simple geometries in Figure 9 are considered for testing the porosity model. The first case is a cube with a single porosity region which solidifies uniformly from the outer surface. A 3D transient temperature-solid fraction field is imposed to provide the test conditions for this casting. The material properties and model parameters used in all test cases are listed in Table 2. Simulation results for the first case are shown in Figure 10. After 1 second from the start of the test case simulation ($\text{Time} = 1\text{s}$ in the plots in Figure 10), a porosity region nucleates at the center of the block, where the solid-fraction is the lowest (Figure 10(a)). After nucleation, liquid in the forming porosity region feeds the shrink in the casting without noticeable pressure drop in the mushy zone. At this stage, the total liquid pressure distribution is almost hydrostatic everywhere in the casting (Figure 10(b)). Results at 45 s show that the porosity region grows from 1 to 45 s (Figure 10(f)). Also observe that the liquid pressure drops, and the flow direction is towards the corners (Figure 10(e)). The liquid pressure drop results from higher flow resistance in those areas due to the higher solid-fraction values at the corners (Figure 10(d)). Finally, at 90 s the block is mostly solidified (Figure 10(g)) and there is almost no feeding flow in the casting. Thus, the dynamic pressure inside the porosity region is uniform which causes the total pressure to become hydrostatic; while, in the solid areas the pressure is set to a low value (Figure 10(h)). The maximum porosity value is observed at the center of the block at the end of this test case simulation as one would expect for such an idealized hot spot in a casting (Figure 10(i)).

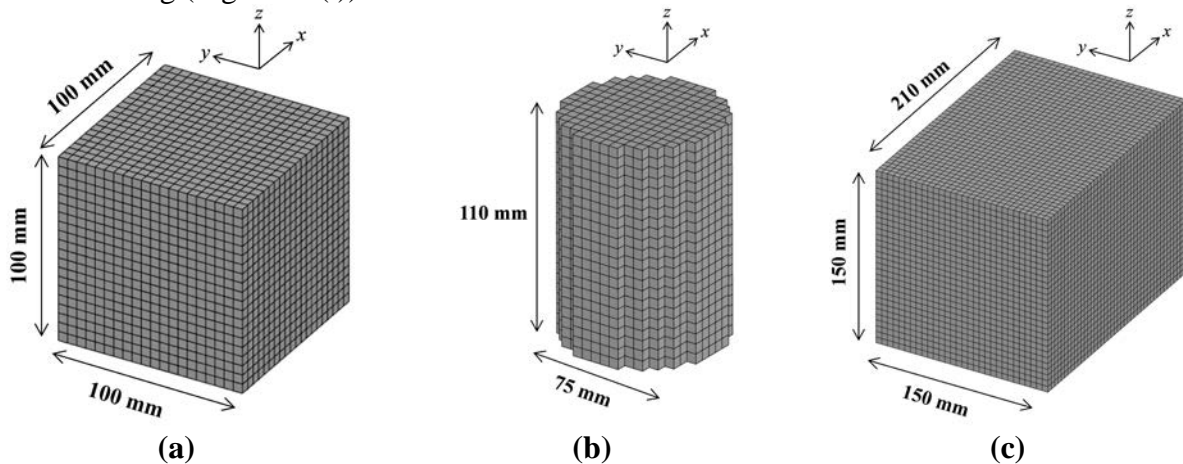**(a)**   **(b)**   **(c)**

Figure 9. Geometries of model test cases: (a) a block with single feeding zone, (b) a riser with surface sink and internal porosity, and (c) block with two feeding zones.

Table 2. Properties and model parameters used in simulations

Parameter	Value (Test Cases)	Value (Mn-Steel Castings)
$K_0 \, (\text{m}^2)$	1×10^{-8}	1.7×10^{-9}
$K_{\min} \, (\text{m}^2)$	5×10^{-15}	1×10^{-16}
$K_{\max} \, (\text{m}^2)$	4×10^{-6}	1×10^{-6}
$g_{s,sur} \, (-)$	0.50	0.55
$g_{s,coh} \, (-)$	0.50	0.55
$\varepsilon_{layer} \, (-)$	1×10^{-2}	3.5×10^{-2}
$\varepsilon_{nuc} \, (-)$	1×10^{-2}	1×10^{-3}
$P_{atm} \, (\text{bar})$	1.01325	1.01325
$P_{\sigma,0} \, (\text{bar})$	P_{atm}	P_{atm}
$P_{mold} \, (\text{bar})$	P_{atm}	P_{atm}
$\rho_{solid} \, (\text{kg/m}^3)$	7124	7124
$\rho_{liquid} \, (\text{kg/m}^3)$	6958	6958
$\mu_\ell \, (\text{Pa.s})$	5×10^{-3}	5.63×10^{-3}

A parametric study was performed for this case to investigate the effects of model parameters on the final porosity results. Its results are given in Figure 11. The study investigated the effects of the model parameters ε_{layer}, ε_{nuc}, $g_{s,sur}$ and $g_{s,coh}$ on the formation of porosity for the test case. For $\varepsilon_{layer} = 0.001$ the porosity in the block is somewhat more concentrated in the center with dispersed porosity biased towards the top of the casting (Figure 11(a)). While for the larger value $\varepsilon_{layer} = 0.10$, the shrinkage porosity appears uniformly spread around the open hole centered in the block (Figure 11(b)). The parameter ε_{nuc} controls the size of the nucleation region in the casting. For $\varepsilon_{nuc} = 0.001$ the internal porosity nucleates in relatively small area at the center of the block (Figure 11(c)) and a larger value of $\varepsilon_{nuc} = 0.10$ results in more uniformly dispersed porosity at the casting's center (Figure 11(d)). Lastly the effect of the critical solid fractions, $g_{s,sur}$ and $g_{s,coh}$ were investigated. Simulation results show that a lower value of $g_{s,sur} = g_{s,coh} = 0.25$ leads to smaller open hole at the block's center (Figure 11(e)) than for a larger value of $g_{s,sur} = g_{s,coh} = 0.75$, which results in a larger open hole in the block (Figure 11(f)). When larger values of $g_{s,sur}$ and $g_{s,coh}$ are used, the solid network structure becomes coherent at higher solid-fractions. This results in pores having more time to grow and form an open hole in the casting.

In the second test case a cylindrical riser shown in Figure 9(b) was simulated. In order to create a more noticeable shrinkage pipe in the casting, the solid density was increased to $\rho_{solid} =$ 7798 kg/m^3 from the first test case. Simulation results for solid fraction, total pressure and porosity are given in Figure 12 at 1, 100, 160 and 210 seconds after the start of the simulation. At the beginning of solidification, a surface sink forms at the top of the riser. Liquid drains from the top of the riser feeding all shrinkage in the casting until around 160 seconds (Figures 12(a)-(f)). During the period before 160 seconds, the total pressure distribution is essentially hydrostatic in the casting, and the flow is from the surface sink toward the solidifying regions (Figures 12(b) and (e)). After around 160 seconds, the surface becomes coherent and stops sinking. Subsequently, internal porosity nucleates adjacent to the surface sink and keeps growing until the end of solidification (Figures 12(g)-(l)). After 160 seconds, the magnitude of the total liquid pressure is much lower compared to the earlier stage due to the low pore pressure (note the scale change in Figures 12(h) and 12(k)). It is observed that as the flow moves toward the solidifying regions, and the pressure drops significantly due to the flow resistance in solid network as shown in Figure 12(h). After the casting is fully solidified, a shrinkage pipe from the top surface and then internal porosity are observed in the casting in Figure 12(l).

In the third test case temperature and solid fraction fields are prescribed creating two feeding zones in the casting, as seen in the solid fraction field plot in Figure 13(a). Based on the results presented in Figure 13, two porosity regions nucleate at the locations with lowest solid-fraction in the casting (Figures 13(a) and 13(c)). These two porosity regions feed the shrinkage volume in the casting and grow until the end of solidification (Figures 13(g) to 13(i)). Note that the flow direction is away from the regions of largest porosity and towards the solidifying regions (Figures 13(b) and 13(e)). Also note the total liquid pressure drop in areas with high solid-fraction during solidification in Figures 13(b) and (e).

These simple test cases demonstrate that the model predicts the expected formation of porosity in hot spots of castings, riser shrinkage piping and that it works for multiple feeding zones with hot spots. Previously, it has been observed that porosity predictions have a feeder shrinkage piping appearance even for castings with hot spots, as in the first and third cases discussed here. Also, because the model accounts for the effects of pressure in the casting, it will be capable of modeling the feeding capabilities of blind risers, which current porosity models cannot reliably predict.
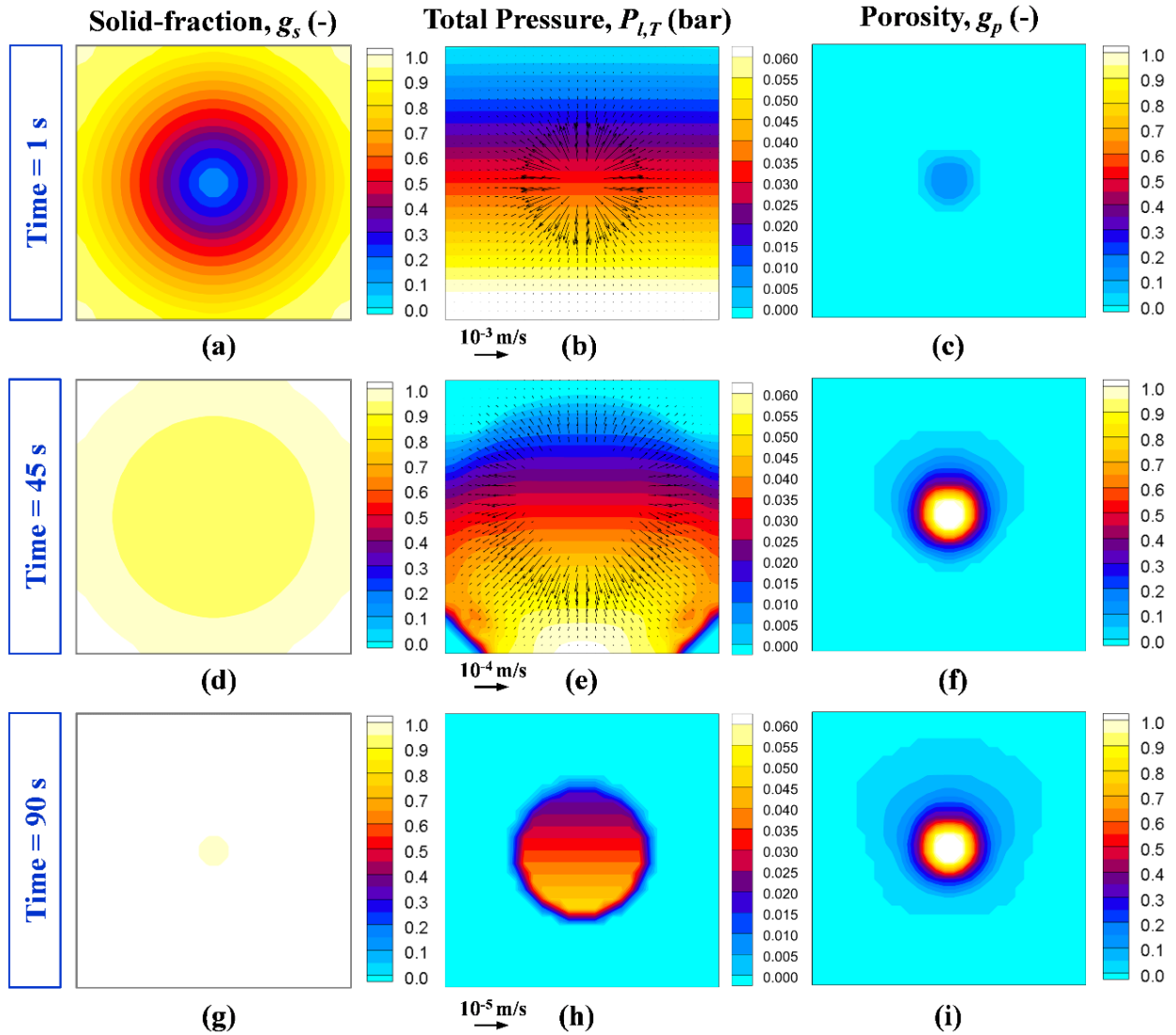
Figure 10. Mid-plane simulation results for the block: the solid-fraction (first column), the liquid pressure (second column) and the porosity (third column) distributions: (a)-(c) at 1 s, (d)-(f) at 45 s, (g)-(i) at 90 s.
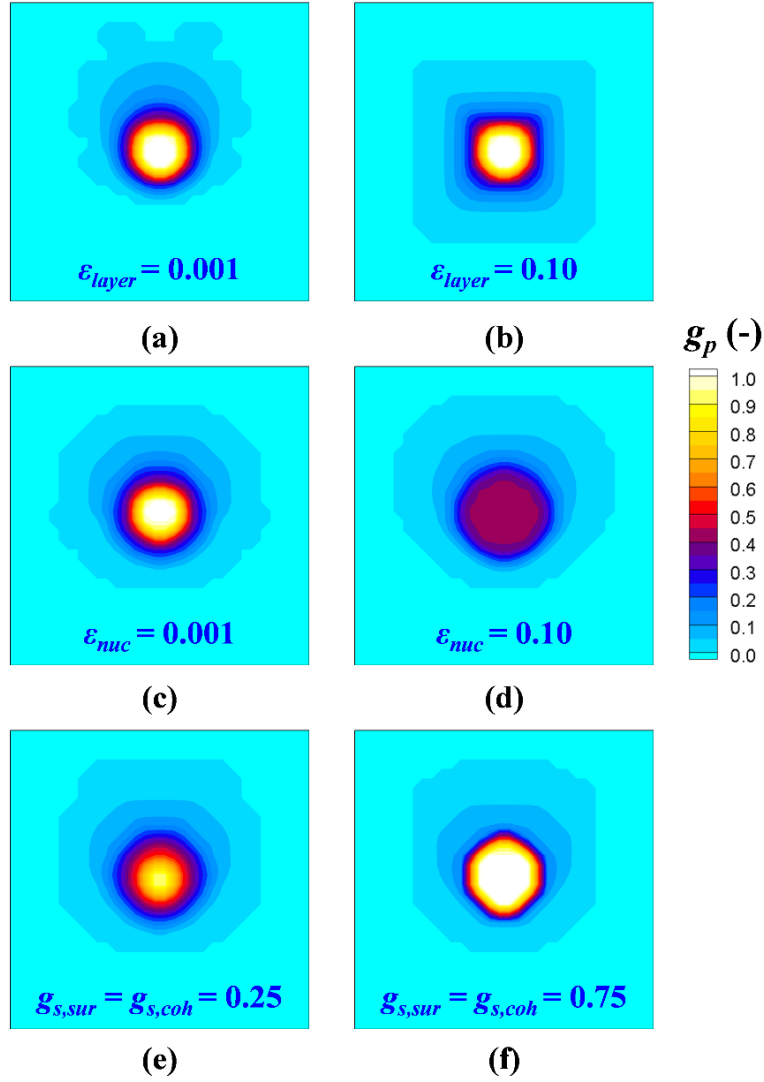
Figure 11. Mid-plane simulation results for the parametric study: (a) $\varepsilon_{layer} = 10^{-3}$, (b) $\varepsilon_{layer} = 1 \times 10^{-1}$, (c) $\varepsilon_{nuc} = 10^{-3}$, (d) $\varepsilon_{nuc} = 10^{-1}$, (e) $g_{s,sur} = g_{s,coh} = 0.25$, (f) $g_{s,sur} = g_{s,coh} = 0.75$.
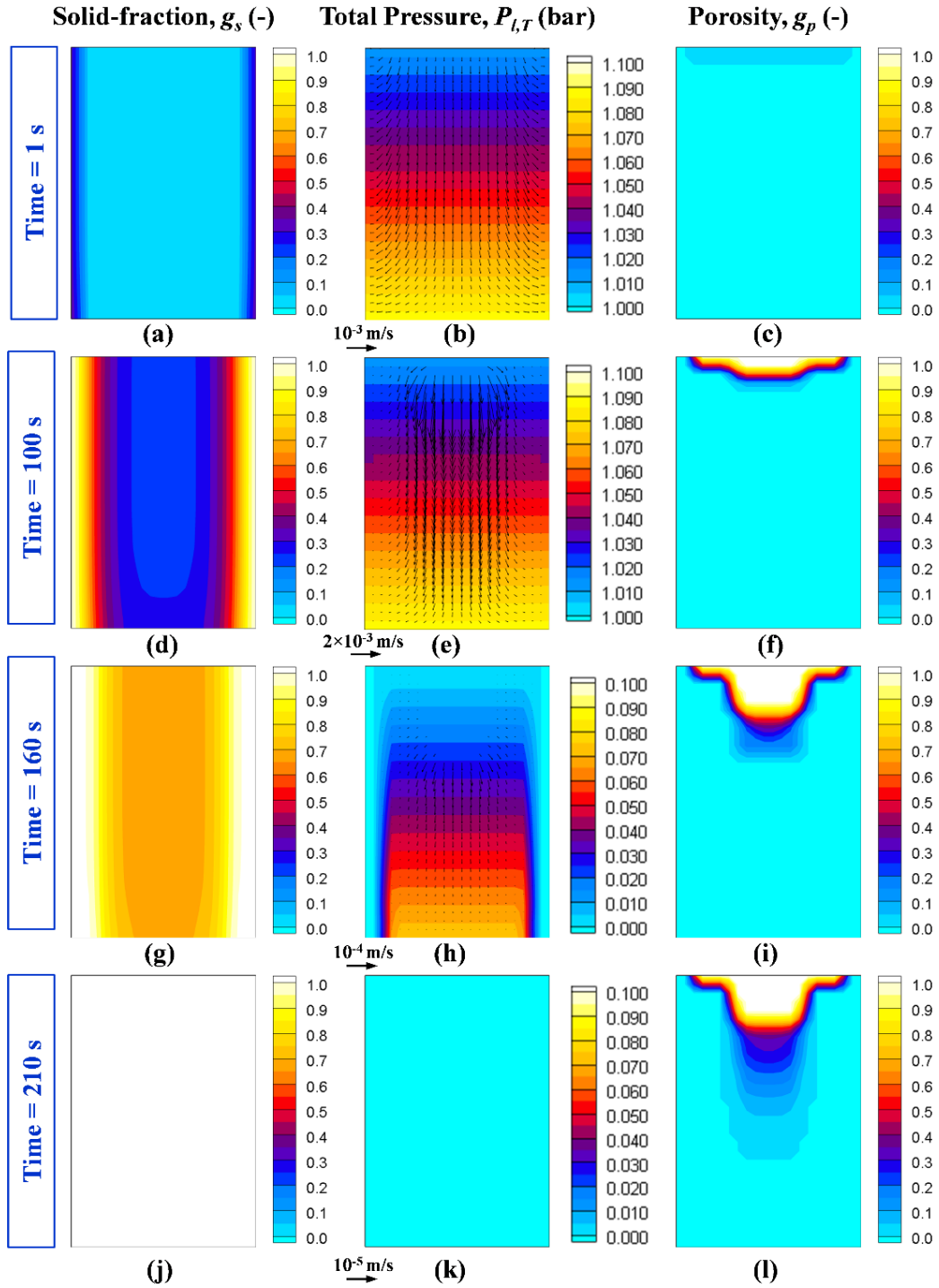
Figure 12. Mid-plane simulation results for the cylindrical riser case showing the solid-fraction (first column), the liquid pressure (second column) and the porosity (third column) distributions at four times from the simulation start (a)-(c) 1 s, (d)-(f) 100 s, (g)-(i) 160 s, and (j)-(l) 210 s.
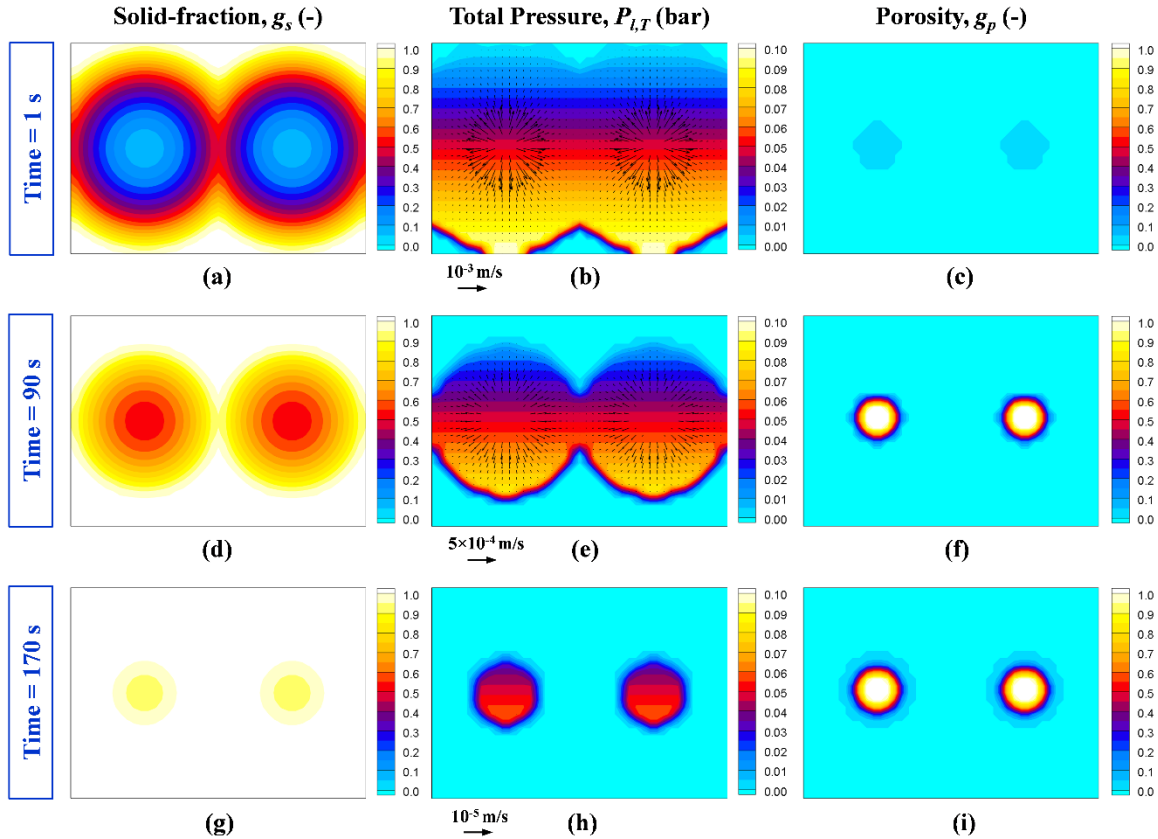
Figure 13. Mid-plane simulation results for the test case with two porosity regions showing the solid-fraction (first column), the liquid pressure (second column) and the porosity (third column) distributions at (a)-(c) 1 s, (d)-(f) 90 s, and (g)-(i) 170 s from simulation start.

4.2. Model Application to Mn-Steel Castings

The first Mn-steel experiment presented here (shown in Figure 4(a)) was modeled using the parameters in Table 2. Solid fraction, total pressure and porosity results for the model are given in Figures 14 and 15. All times referenced below, for both Mn-steel experiments, are seconds (s) from the start of the simulation. At 10 s the casting is mostly liquid as shown in Figures 14(a) and 15(a), and a porosity region forms at the top surface of the poring cup (Figure 14(c)) and feeds the developing shrinkage in the entire casting. The total liquid pressure distribution is hydrostatic and the flow direction is away from the pouring cup towards the downsprue/runner in Figures 14(b) and 15(b). The surface sink in the pouring cup grows until around 150 s, when it becomes coherent stops developing. Around 150 s another surface sink nucleates at the top of the riser, and begins compensating for the volumetric shrinkage in the system. A shrinkage pipe forms in the riser (Figures 14(f) and 15(f)). The shrinkage pipe in the riser develops, and around 300 s a large pressure drop develops in the block-shaped hot spot section at the end of the casting opposite the feeder (Figure 15(h)) and internal porosity nucleates there (Figure 15(i)). After 300 s, both the developing riser shrinkage pipe and the internal porosity in the block-shaped hot spot section feed

the shrinkage in the casting. As the solid fraction increases along the thinnest section of the casting, the liquid pressure drops significantly from 300 to 1650 s (Figure 15(h)), which leads to the formation of a centerline porosity along the thinnest section of the casting as indicated in Figure 15(l). Porosity ceases forming when the casting is fully solidified. A comparison between the experimentally observed porosity and the porosity predicted by the model are shown on the mid-width plane of the casting in Figure 16. The experimentally observed macroporosity (visible without magnification) and microporosity (revealed by dye penetrant test) are shown for both halves of the casting in Figure 16. These results show that the model realistically predicts the amount and appearance of shrinkage porosity from the experiment that forms in the thin section centerline, in the hot spot section, and in the riser shrinkage pipe.

The simulation results for the Mn-steel Experiment 2 showing solid fraction, total pressure and porosity are presented in Figure 17 and Figure 18. At 10 seconds from the start of solidification, again the casting is mostly liquid as shown in Figures 17(a) and 18(a), and a surface porosity region forms at the top of the pouring cup (Figure 17(c)), which feeds the developing shrinkage for the entire casting system. The liquid pressure in Figures 17(b) and 18(b) is hydrostatic. The directions of flow are from the top of the pouring cup towards the downsprue and from the riser into the runner in these figures. The pouring cup surface sink grows until around 150 s. At this point the top surface of the cup becomes coherent as seen in Figure 17(d). Subsequently, the shrinkage pipe stops forming in the cup and downsprue, and another surface sink forms on the top surface of the riser, which provides feed metal to the casting volume shrinkage (Figures 17(f) and 18(f)). This feeding condition continues until around 500 when the flow resistance in the thin section of the plate increases resulting in nucleation of internal porosity in the hot spot block (Figure 18(i)). Following this, internal porosity in the riser and thin plate section, and internal porosity in the hot spot, feed the remaining volumetric shrinkage in the casting system (Figures 18(j) to 18(l)). Flow from the hot spot and riser cannot feed the thin section of the plate, and a centerline shrink forms in this area (Figure 18(l)). Surface sinks and shrinkage porosities stop growing once the casting is fully solidified. Comparisons between simulation and experiment in Figure 19 demonstrate that the feeding model can faithfully predict the formation of shrinkage porosity in Mn-steel casting. The results, though similar to Experiment 1, show a vertical riser shrinkage pipe in the experimentally observed and the simulated Experiment 2 casting. For Experiment 1 both the predicted and observed shrinkage pipes in the riser appear to bend toward the casting. In both cases, the model agrees with experimental observations.

Studies were performed to investigate the effects of model parameters on predicted porosity distribution. Results from these parametric studies are presented in Figures 20 and 21. The results in Figures 20(a) and 21(a) reveal that increasing ε_{layer} from 0.01 to 0.10 affects the shape of shrinkage pipe in the riser, while only producing a minor effect on the internal porosity distribution in the casting. Simulations in Figures 20(b) and 21(b) show that varying ε_{nuc} between the same values is insignificant on the shrinkage pipe prediction, but it affects the appearance of the internal porosity. A larger value of ε_{nuc} disperses the internal porosity over the center part of the hot spot, and the smaller value of ε_{nuc} concentrates this internal porosity. The effects of $g_{s,sur}$ and $g_{s,coh}$ on the porosity distribution are shown Figures 20(c) and 21(c). Observe that increasing these parameters from $g_{s,sur} = g_{s,coh} = 0.45$ to $g_{s,sur} = g_{s,coh} = 0.60$ changes only slightly the shape

and the size of shrinkage pipe in the riser. Also varying these parameters in this range has a negligible effect on the internal porosity distributions in the hot spots and thin sections. The effects of K_0 and K_{min} are presented Figures 20(d), 20(e), 21(d) and 21(e). These results indicate that decreasing the values of K_0 and K_{min} increase and diffuse the pressure-drop during solidification which results in large more disperse porosity regions, when compared to larger values of K_0 and K_{min}. Also the effects of mold and capillary pressure conditions were investigated. In Figures 20(f) and 21(f), the effects of changing P_{mold} are presented. These results illustrate that this parameter is only important in the formation of surface sink (note top surface of riser in Figure 20(f)), and that almost no effect is observed on the internal porosity. The effect of the capillary pressure condition P_σ on the porosity formation is presented in Figures 20(g) and 21(g). These results demonstrate that increasing P_σ from $0.5 P_{atm}$ to $2.0 P_{atm}$ significantly alters the shape and distribution of shrinkage pipe in the riser, and also the internal porosity distributions in the thin and hot spot sections are more disperse when $P_\sigma = 0.5 P_{atm}$.
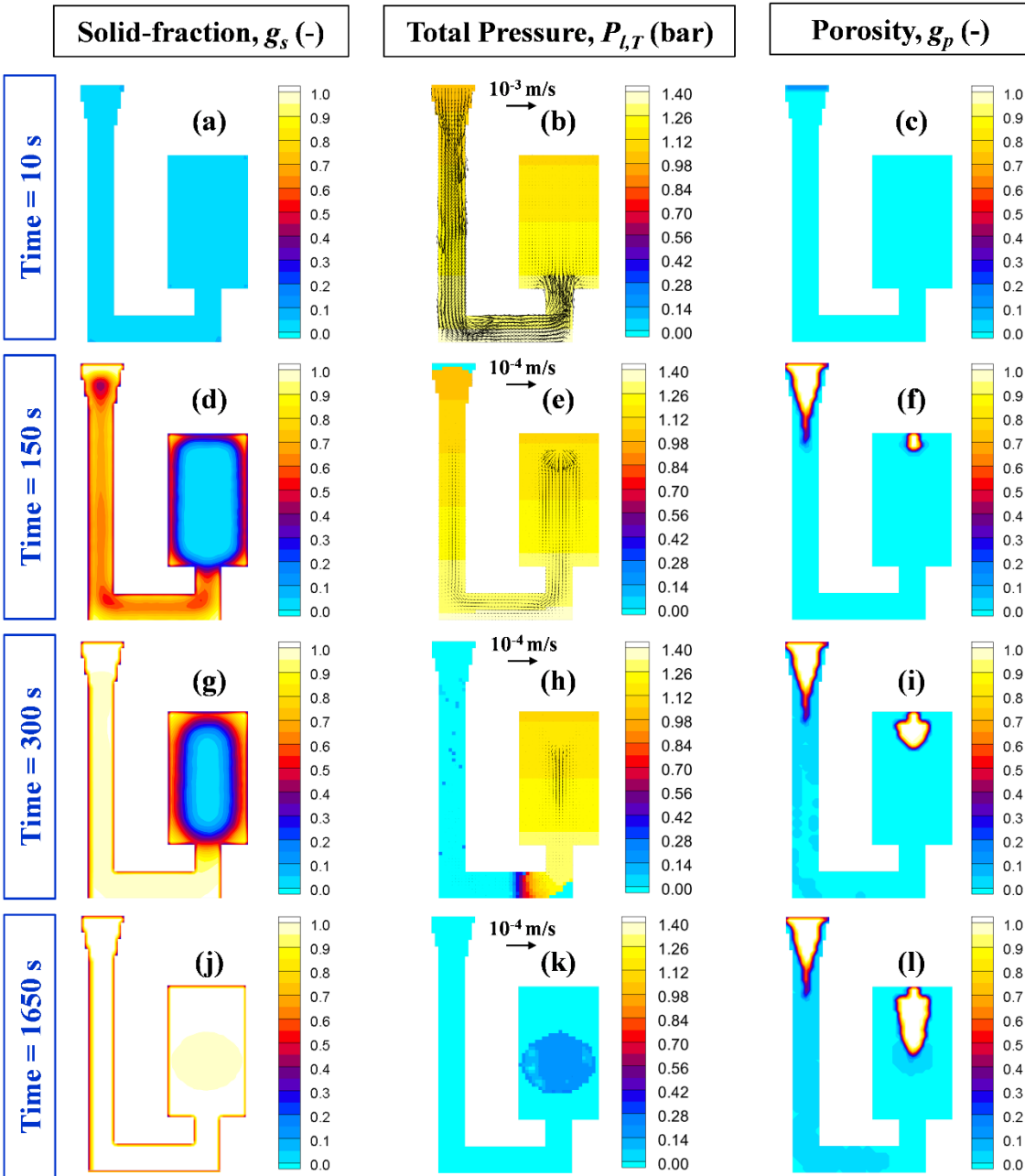
Figure 14. Mid-riser simulation results for Mn-steel casting showing the solid-fraction (first column), the liquid pressure (second column) and the porosity (third column) distributions at (a)-(c) 10 s, (d)-(f) 150 s, (g)-(i) 300 s, and (j)-(l) 1650 s from the start of the simulation.
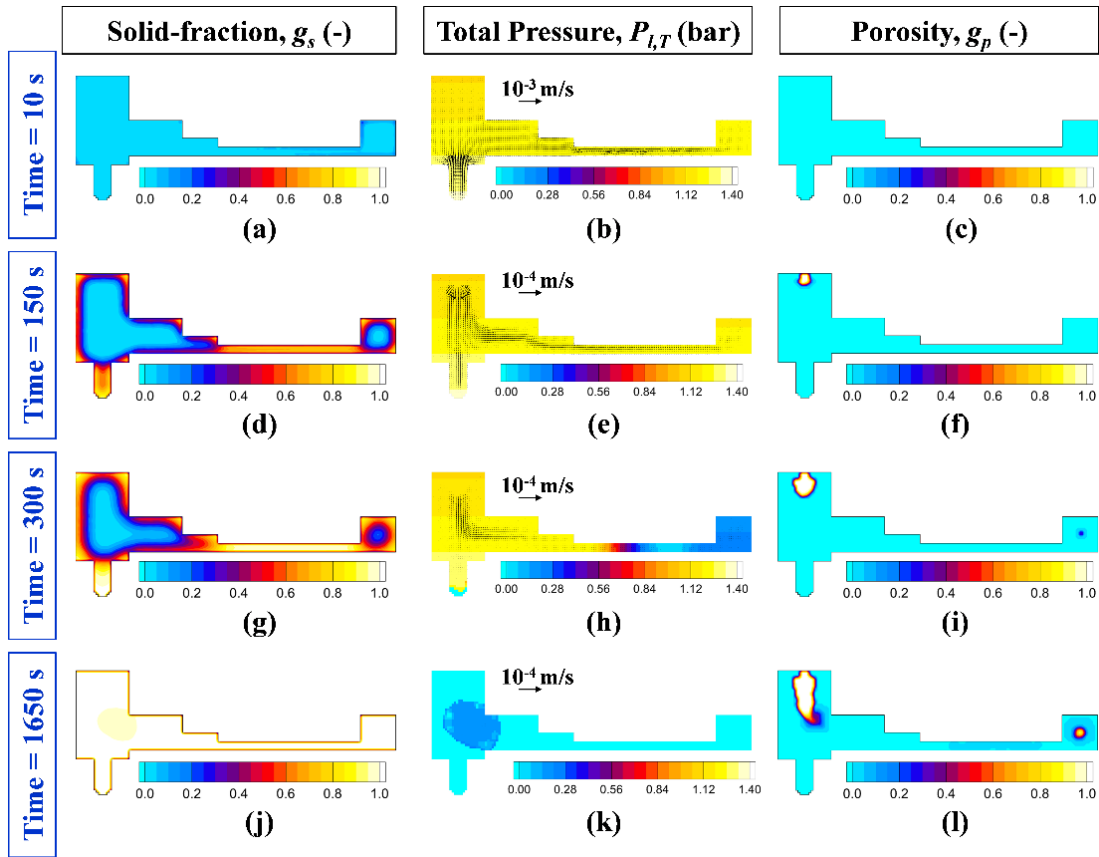
Figure 15. Mid-plane simulation results for Mn-steel casting showing the solid-fraction (first column), the liquid pressure (second column) and the porosity (third column) distributions at (a)-(c) 10 s, (d)-(f) 150 s, (g)-(i) 300 s, and (j)-(l) 1650 s from the start of the simulation
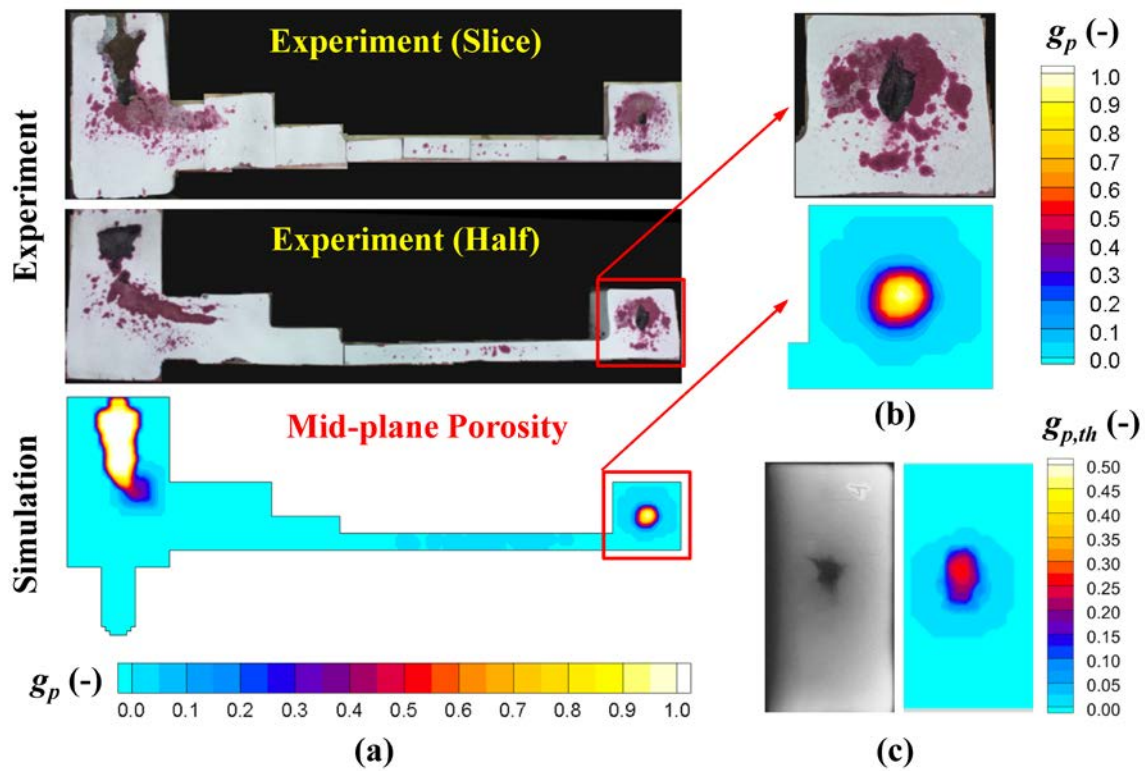
Figure 16. (a) and (b) Porosity distribution observed and predicted on the mid-plane of Mn-steel casting Experiment #1, and (c) top view of radiograph and predicted through thickness porosity for hot spot feature detailed in (b).
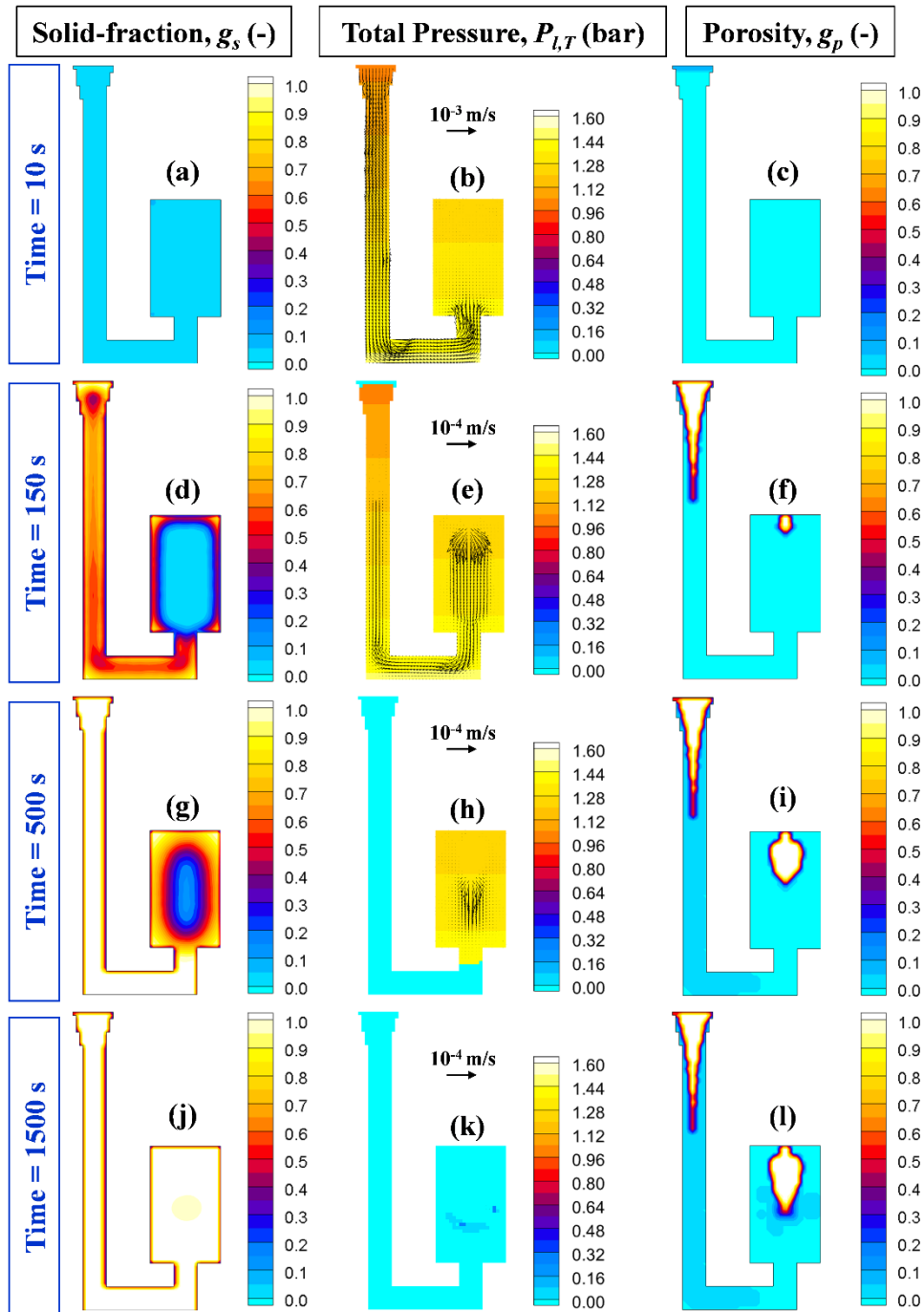
27

Figure 17. Mid-riser simulation results for Mn-steel casting showing the solid-fraction (first column), the liquid pressure (second column) and the porosity (third column) distributions at (a)-(c) 10 s, (d)-(f) 150 s, (g)-(i) 500 s, and (j)-(l) 1500 s from the start of the simulation.
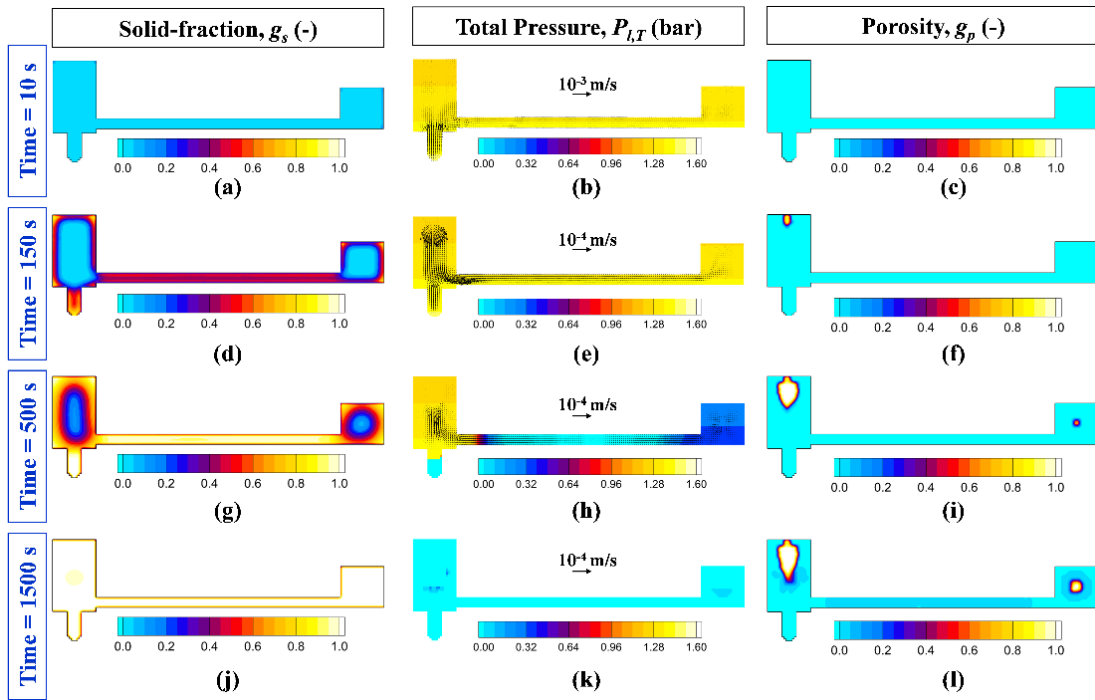
Figure 18. Mid-plane simulation results for Mn-steel casting showing the solid-fraction (first column), the liquid pressure (second column) and the porosity (third column) distributions at (a)-(c) 10 s, (d)-(f) 150 s, (g)-(i) 500 s, and (j)-(l) 1500 s from the start of the simulation.
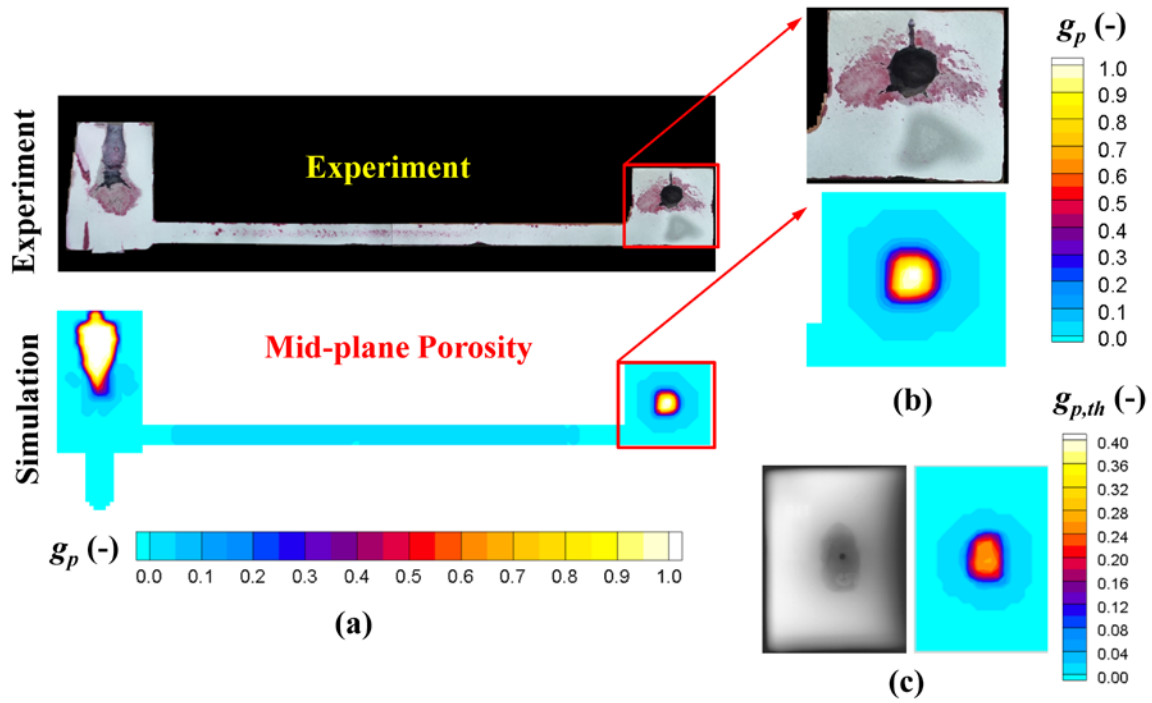
Figure 19. Comparison of experimental results with predictions in Mn-steel casting: (a)-(b) mid-width section porosity distributions, (b) porosity distribution on the mid-width section of the block, and (c) top view X-ray results and predicted through thickness porosity for hot spot in (b).
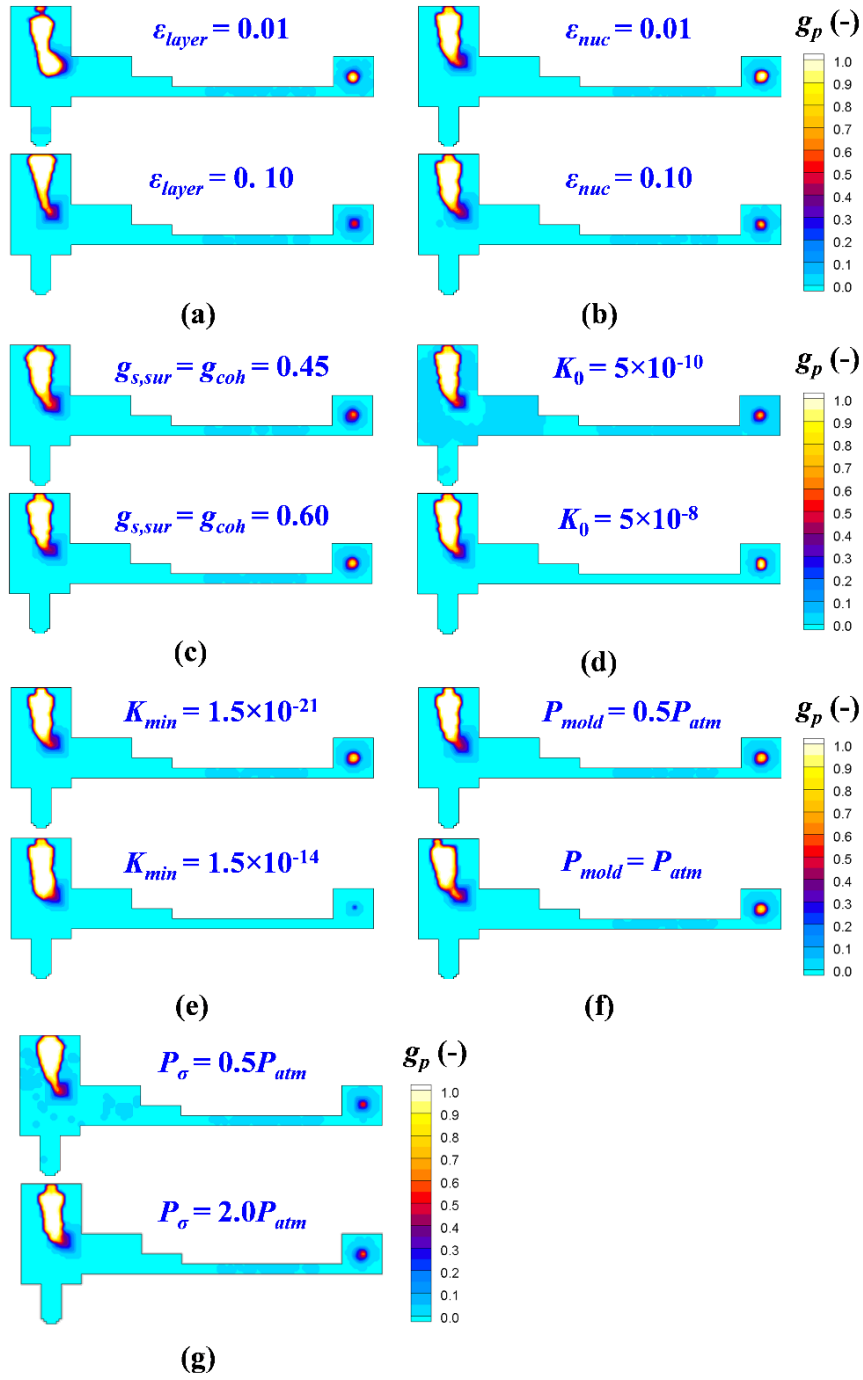
Figure 20. Simulation parametric study results on the mid-width section of the Mn-steel experiment 1: (a) effect of ε_{layer}, (b) effect of ε_{nuc}, (c) effect of $g_{s,sur}, g_{s,coh}$, (d) effect of K_0, (e) effect of K_{min}, (f) effect of P_{mold} and (g) effect of $P_{\sigma,0}$.
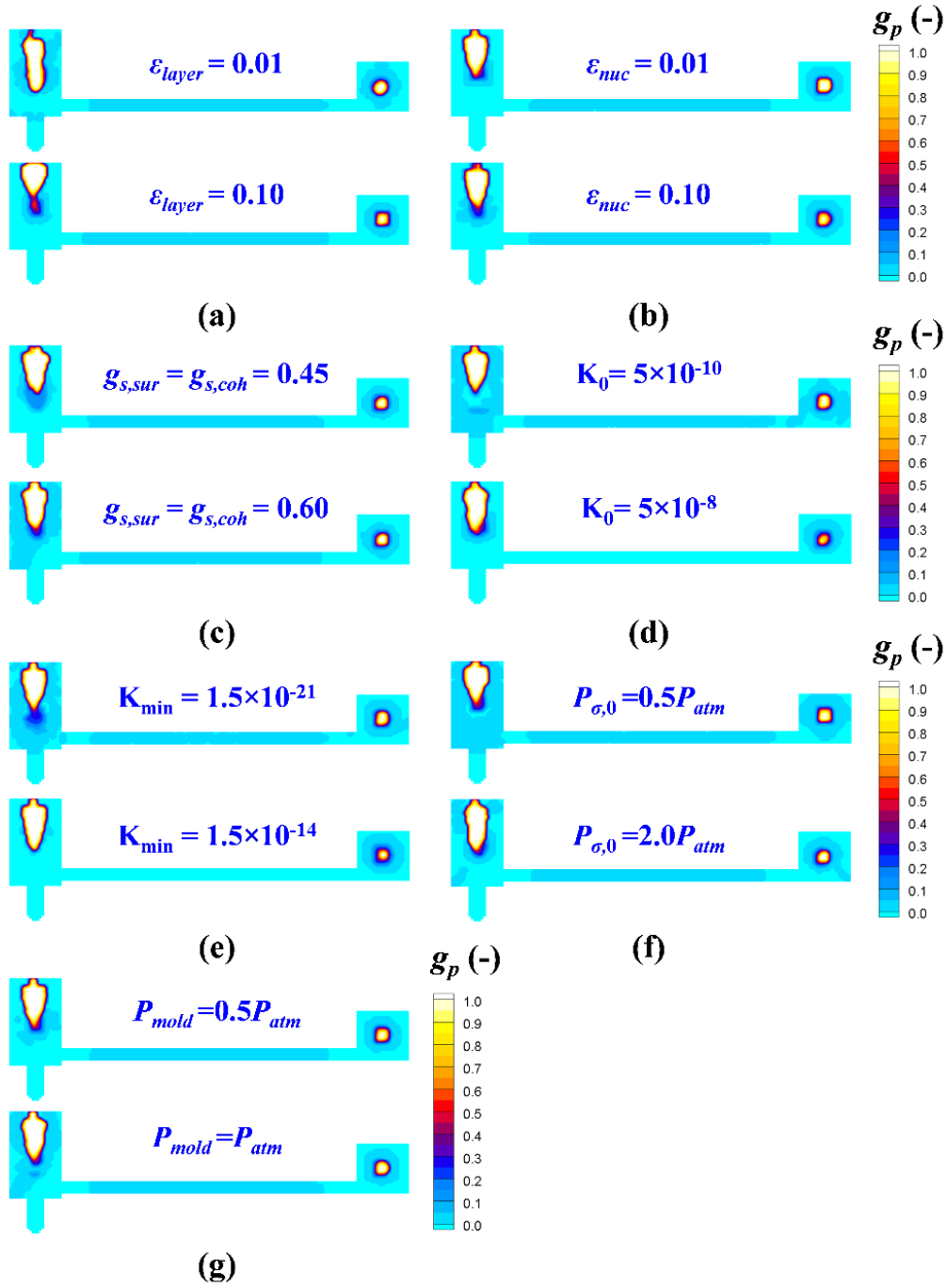
Figure 21. Simulation parametric study results on the mid-width section of the Mn-steel experiment 2: (a) effect of ε_{layer}, (b) effect of ε_{nuc}, (c) effect of $g_{s,sur}, g_{s,\mathrm{coh}}$, (d) effect of K_0, (e) effect of $K_{\min}$, (f) effect of P_{mold} and (g) effect of P_σ.

5. CONCLUSIONS

Porosity in steel castings reduces the mechanical performance of cast components by adversely affecting the material's mechanical, fatigue, and creep properties. Microporosity, which can be difficult to detect, also causes leaks in pressure containing castings. By predicting these defects in casting process simulation, the process can be designed to avoid or eliminate them resulting in fewer scrapped castings, increased casting yield and higher performing cast components. Here recent advances have been presented in the development, validation and application of a casting simulation model that provides improved predictions of porosity.

The model implements a unified approach to predicting macro-shrinkage porosity, surface sink and micro-shrinkage porosity. The model was developed to more accurately predict the location, amount and appearance of porosity. Porosity predictions are demonstrated for simple casting geometries, and for more complex experimental castings. Results for simple geometries predict that at the early stages of the solidification, when the casting surfaces are not coherent, the shrinkage defects appear in the form of surface sinks on the casting's exterior. Once the surfaces become rigid, internal porosity nucleates and develops in areas with low solid fractions. The model was then applied to Mn-steel castings. Current porosity models have difficulties accurately predicting porosity for high Mn-steels. The model results are compared to two experiments. In the experiments the cooling of castings was measured by several thermocouples located at different areas in mold walls and castings during solidification. Temperature dependent thermo-physical properties were developed for the Mn-steel and Olivine mold used through inverse modeling, where agreement is obtained between measured and simulated temperatures. Comparisons between the porosity model results and the experimentally observed porosity demonstrate the promise and capability of this new model to predict surface and internal shrinkage porosity, micro- and macro- shrinkage porosity, and centerline shrinkage porosity. The effect of model parameters on the predicted porosity is presented. The parametric studies show how the predicted porosity distribution changes depending on model parameters such as: the surface coherency limit ($g_{s,sur}$), mass feeding critical solid-fraction ($g_{s,coh}$), nucleation and distribution parameters ($\varepsilon_{nuc}, \varepsilon_{layer}$), the permeability coefficient (K_0), minimum permeability (K_{min}) and the capillary pressure coefficient ($P_{\sigma,0}$). The parametric studies demonstrate how the model parameters might be tuned to predict the porosity casting alloys. Using the model it is found that the predicted porosity location and its appearance more closely mirrors observed porosity than current simulation capability. In addition, it can be applied to model the feeding characteristics of blind risers, which current porosity models have difficulty predicting.

REFERENCES

[1]. M. J. Couper, A.E. Neeson, and J.R. Griffiths: *Fatigue Fract. Eng. Mater. Struct.*, 1990, vol. 13, pp. 213-27.

[2]. Q.G. Wang, D. Apelian, and D.A. Lados: *J. Light Met.*, 2001, vol. 1, pp. 73–84.

[3]. R.A. Hardin and C. Beckermann: *Metall. Mater. Trans. A*, 2013, vol. 44A, pp. 5316–32

[4]. T.S. Piwonka and M.C. Flemings: *Trans. AIME*, 1966, vol. 236, pp. 1157–65

[5]. K. Kubo and R.D. Pehlke: *Metall. Trans. B*, 1985, vol. 16, pp. 359-366.

[6]. C. Pequet, M. Gremaud, and M. Rappaz: *Metall. Mater. Trans.*, 2002, vol. 33A, pp. 2095–2016.

[7]. K.D. Carlson, Z. Lin, R.A. Hardin, and C. Beckermann: *56th Steel Founders Society of America Technical and Operating Conference*, Paper No. 4.4, Steel Founders' Society of America, Chicago, IL, 2002

[8]. K.D. Carlson, Z. Lin, and C. Beckermann: *Metall. Mater. Trans. B*, 2007, vol. 38 (4), pp. 541–55.

[9]. K.D. Carlson and C. Beckermann: *Metall. Mater. Trans. A*, 2009, vol. 40A, pp. 163–175.

[10]. A. Reis, Y. Houbaert, Z. Xu, R. Van Tol, A.D. Santos, J.F. Duarte, and A.B. Magalhaes, *J. Mater. Process. Tech.*, 2008, vol. 202, pp. 428-434.

[11]. A. Reis, Z. Xu, R.V. Tol, and R. Neto, *J. Manuf. Process.*, 2012, vol. 14, pp. 1-7.

[12]. C. Pequet, M. Gremaud, and M. Rappaz: *Metall. Mater. Trans.*, 2002, vol. 33A, pp. 2095–2106.

[13]. Carlson, K.D., and Beckermann, C., *Int. J. Cast Metals Research*, 2012, Vol. 25, pp. 75-92.

[14]. J. Miettinen, S. Louhenkilpi, H. Kytönen and J. Laine: *Math. Comp. Simul.*, 2010, vol. 80, pp. 1536-50.

[15]. *JMatPro*, Sente Software Ltd., Surrey Technology Centre, Surrey GU2 7YG, United Kingdom.

[16]. H. Samet, and M. Tamminen. *IEEE Transactions on Pattern Analysis and Machine Intelligence*, 1988, vol. 10(4), pp. 579-586.